Fluid inclusion characteristics and molybdenite Re-Os geochronology of the Qulong porphyry copper-molybdenum deposit, Tibet

Yang Li[1†], David Selby[1], Martin Feely[2], Alessandra Costanzo[2], Xian-Hua Li[3]

[1] Department of Earth Sciences, Durham University, DH1 3LE, Durham, UK

[2] Earth and Ocean Sciences, National University of Ireland, Galway, Ireland

[3] State Key Laboratory of Lithospheric Evolution, Institute of Geology and Geophysics, Chinese Academy of Sciences, Beijing, 10029, China

[†] Corresponding author Email, li.yang@durham.ac.uk; cugliyang@126.com.

Abstract

The Qulong porphyry copper and molybdenum deposit is located at the southwest margin of the Lhasa Terrane and in the eastern region of the Gangdese magmatic belt. It represents China's largest porphyry copper system, with ~2200 million tonnes of ore comprising 0.5 percent Cu and 0.03 percent Mo. The mineralization is associated with Miocene granodiorite, monzogranite and quartz-diorite plutons, which intruded into Jurassic volcanic units in a post-collisional (India-Asian) tectonic setting. Field observations and core logging demonstrate the alteration and mineralization at Qulong are akin to typical porphyry copper systems in subduction settings, which comprise similar magmatic-hydrothermal, potassic, propylitic and phyllic alteration assemblages. Molybdenite Re-Os geochronology confirms the relative timeframe defined by field observations and core logging, and indicates that the bulk copper and molybdenum at Qulong were deposited within 350,000 years: between 16.10 ± 0.06 [0.08] (without and with decay constant uncertainty) and 15.88 ± 0.06 [0.08] Ma. This duration for mineralization is in direct contrast to a long-lived intrusive episode associated with mineralization based on previous zircon U-Pb data.

Our fluid inclusion study indicates that the ore-forming fluid was oxidized and contained Na, K, Ca, Fe, Cu, Mo, Cl and S. The magmatic-hydrothermal transition occurred at ~425^{o}C under lithostatic pressure; while potassic, propylitic and phyllic alteration occurred at hydrostatic pressure with temperature progressively decreasing from 425 to 280 ^{o}C. The fluid inclusion data presented here suggests that there has been ~2.3 km of erosion at Qulong after its formation and this erosion may be related to regional uplift of the Lhasa Terrane.

Keywords

Fluid inclusion, Molybdenite Re-Os, Qulong, porphyry deposit, Tibet

Introduction

The majority of porphyry copper deposits are situated within magmatic arcs and are genetically related to subduction processes, e.g., Central Chile (Cooke et al. 2005), but porphyry copper deposits are also associated with post-collisonal tectonic settings, e.g., the Gangdese Porphyry Copper Belt (GPCB), China (Yang et al. 2009; Hou et al. 2015) and Papua New Guinea-Irian Jaya (Cooke et al. 2005; Richards 2013). In both subduction-related and post-collisional tectonic settings, porphyry copper deposits share a genetic association with magmatism and possess similar mineralization styles and alteration types (Richards 2009; Hou et al. 2015).

Metals in porphyry copper deposits are considered to be deposited through the dynamic evolution of a magmatic-hydrothermal fluid that undergoes depressurization, cooling, chemical reactions with wall rocks (mainly the ore-hosting granite), and mixing with non-magmatic fluids (Seedorff et al. 2005; Richards 2011; Cooke et al. 2014). As a result, porphyry systems are characterized by extensive vein formation associated with mineralization and alteration. Generally, hydrothermal alteration results in potassic, propylitic, sericitic (phyllic) and argillic assemblages, which are documented to occur as concentric alteration halos around the ore progenitor intrusions (Seedorff et al. 2005; Sillitoe 2010). Fluid trapped by quartz and other host minerals during alteration and mineralization processes has a wide range of compositions, and is the only record of the ore-forming fluid (Bodnar et al. 2014). As such, fluid inclusions provide fundamental information on the physical and chemical nature of ore-forming fluids. This is critical for understanding the nature and transportation-deposition mechanisms of ore-forming fluids in porphyry copper deposits (Wilkinson 2001; Bodnar et al. 2014).

Additional fundamental questions regarding porphyry deposits include the time required to form these giant deposits and whether the metals accumulate in a single pulse or over several pulses (Chiaradia et al. 2014). The current methods used to constrain time-scales of

porphyry systems include: 1) Ti in quartz diffusion and thermal numerical modelling (Cathles et al. 1997; Weis et al. 2012; Mercer et al. 2015); 2) calculation from metal concentration and fluid flow in active hydrothermal systems (Simmons and Brown 2006, 2007); and 3) direct radiogenic dating (Sillitoe and Mortensen 2010; Von Quadt et al. 2011; Zimmerman et al. 2014; Spencer et al. 2015). The reported time-scales of fossil porphyry deposits range from <0.1 to >4 m.y. The longer durations may reflect multiple magmatic-hydrothermal pulses or inaccurate dating approaches (e.g. lower precision dating). The development of high-precision geochronology, especially molybdenite Re-Os in recent years has permitted direct dating of the ore forming events associated with porphyry copper systems with precision better than tens of thousands years (Zimmerman et al. 2014; Spencer et al. 2015). As molybdenite is widely distributed in porphyry Cu deposits, Re-Os molybdenite dating is currently the best technique to constrain the ore formation duration of porphyry copper deposits.

Although extensive fluid inclusion research has been conducted to understand ore forming processes for subduction related porphyry deposits (Bodnar et al. 2014 and references therein), much less attention has been paid to post-collisional porphyry deposits (Hou et al. 2009). The world-class Qulong porphyry deposit, Tibet, is an excellent example of a porphyry system formed in a post-collisional tectonic setting (Hou et al. 2015). Qulong was discovered in 1994 with significant exploration success commenced from 2002 (Zheng et al. 2004). This period of exploration uncovered a deposit with ≥2200 million tonnes ore. The average metal grade at Qulong deposit is 0.5 percent for Cu and 0.03 percent for Mo, making it the largest copper bearing porphyry system in China, and among the world's largest (top 25) porphyry copper deposits (Cooke et al. 2005; Yang et al. 2009; Qin et al. 2014). Therefore, to understand both the P-T-V-X conditions of Qulong, and the porphyry systems associated with post-collisional tectonic settings, we present fluid inclusion petrography data coupled with microthermometry and Laser Raman microspectroscopy data. We also present

molybdenite Re-Os geochronology to constrain the timescale of the mineralization event. In addition, zircon U-Pb geochronology and oxygen isotope data allow us to constrain the origin of the syn-ore aplite and the nature of the ore-forming fluids.

Geological setting

Regional geology

The Gangdese porphyry copper belt is 50 km wide and ~400 km long, and is situated at the southwest margin of the Lhasa Terrane, southern Tibet (Fig.1) (Hou et al. 2009). The Lhasa Terrane records a protracted geologic history with a Precambrian crystalline basement underlying Paleozoic to Mesozoic marine strata and arc type volcanic rocks, together with Mesozoic and Cenozoic intrusions (Zhang et al. 2014). The Lhasa Terrane rifted from Gondwana during the Triassic or Middle-Late Jurassic and moved northward across the Neo-Tethyan Ocean before collision with Eurasia along the Bangonghu-Nujiang suture during the Cretaceous (Zhu et al. 2011a,b; Zhang et al. 2014). The continental collision of India and Asia along the Indus-Yarlung Zangbo suture started at ~55 Ma (Rowley 1996), with underthrusting of the Indian plate beginning at ~35 Ma (Ali and Aitchison 2008; Wang et al. 2014a). Continued collision of the Indian and Asian plates resulted in the breakoff of the denser Indian plate beneath the Asian plate from west to east of Tibet at ~25 and ~15 Ma, respectively (Aitchison et al. 2007; Van Hinsbergen et al. 2012). Directly related to slab breakoff was magma generation which resulted in Oligo-Miocene magmatic rocks focused along the Gangdese belt (Hou et al. 2009; Van Hinsbergen et al. 2012; Wang et al. 2014a). The Oligo-Miocene magmatism is consistent spatially linked with N-S trending normal faults formed during E-W extention of the Lhasa Terrane (Hou et al. 2009; Wang et al. 2014a,b). Porphyry copper mineralization is commonly strictly associated with the Oligo-Miocene intrusions in the east segment of the Gangdese porphyry copper belt (Wang et al.

2015), of which the Qulong deposit is not only largest in this belt, but also in China (Zheng et al. 2004; Qin et al. 2014).

Magmatic rocks

The main igneous units present at Qulong include Jurassic volcanic and dacite-rhyolite intrusions, a pre-ore Miocene granite pluton, ore-related Miocene porphyries and aplite intrusions, and a post-ore quartz diorite. Features of these units are summarized in Table 1 and presented below.

Jurassic Yeba Formation and dacite-rhyolite porphyry

The Jurassic Yeba Formation is the most extensive unit in the Qulong district (Fig. 2A) and is comprised of basaltic and felsic lavas. The age of the formation is constrained by a zircon LA-ICP-MS age of 166.0 ± 1.8 Ma in the felsic volcanoclastic rocks (Zhao et al. 2015). The Yeba Formation sequence is intruded by dacite-rhyolite and rhyolite porphyry stocks. These porphyry stocks are composed of quartz (20-25 vol%) and feldspar (8-10 vol%) as phenocrysts, with a quartz, K-feldspar and biotite as groundmass. Zircon grains from the rhyolite porphyry yielded a LA-ICP-MS U-Pb age of 160.7 ± 2.0 Ma (Zhao et al. 2015). Volcanic rocks from the Yeba Formation and the porphyry stocks show geochemical characteristics indicative of an arc-affinity, suggesting an origin related to Mesozoic Neo-Tethyan Ocean subduction (Yang et al. 2008b).

Rongmucuola pluton

The Jurassic Yeba Formation and dacite-rhyolite porphyry units are intruded by the ~8 km^2 Rongmucuola pluton (Fig. 2A and B). At its contact with the Rongmucuola pluton, the Yeba Formation exhibits intensive metamorphism as represented by pervasive hornfels (Yang et al. 2009). From east to west, the composition of the Rongmucuola pluton ranges from

granodiorite to monzogranite (Fig. 3A), and has a variable grain size (medium to coarse), and ranges from being hypidiomorphic-granular to weakly porphyritic (Yang et al. 2009; Zhao et al. 2015). Mafic enclaves are quite common in the eastern portion of the pluton, but are rare in the west (Zhao et al. 2015). Despite the small compositional and textural variations, the entire pluton possesses a similar mineralogy and crystallization age (17.6 ± 0.3 Ma and 17.4 ± 0.4 Ma; zircon LA-ICP-MS U-Pb) (Zhao et al. 2015). The bulk of the Cu-Mo mineralization is hosted in the western part of the pluton that comprises coarse grained (5-10 mm) plagioclase (30-40 vol%), K-feldspar (20-30 vol%), and medium grained (2-5 mm) quartz (15-20 vol%) and biotite (10-15 vol%), and accessory minerals such as apatite, magnetite, zircon, rutile; no titanite has been documented. The pluton is characterized by a porphyritic texture throughout, a progressive increase in alteration intensity from the surface to ~2000 m depth (predominantly silicification and potassic alteration), and exhibits a colour change from dark grey to grey.

P porphyry (monzogranite)

The western part of the Rongmucuola pluton is intruded by the P porphyry (Fig. 2A and B), which is considered to be the ore-forming porphyry (Yang et al. 2009; Hu et al. 2015; Zhao et al. 2015). The P porphyry has an exposure surface of 0.5 km^2, and an unknown vertical extent. The P porphyry comprises coarse grained (3-8 mm) plagioclase (10-20 vol%), quartz (5-15 vol%) and K-feldspar (~5 vol%) as phenocrysts, with a groundmass dominated by quartz and feldspar (Fig. 3B). The porphyry shows extensive alteration and mineralization. The feldspar phenocrysts possess distinctive embayed shapes, with the groundmass displaying different degrees of hypogene argillization as a result of either the complete or partial destruction of feldspar. Characteristic to the P porphyry is its quartz phenocrysts which occur as clusters of two or three and forms amalgamated “phenocrysts” (Fig. 3B). These quartz phenocrysts often show resorbed crystal margins and embayment textures (Fig.

3B) which indicate intense silicification (Chang and Meinert 2004; Yang et al. 2009; Qin et al. 2014). Zircon LA-ICPMS U-Pb analysis yielded a 16.2 ± 0.3 Ma emplacement age for the P porphyry (Zhao et al. 2015).

X porphyry (monzogranite)

In the western portion of the Rongmucuola pluton, the X porphyry occurs with a surface outcrop of ~0.04 km^2; it is also present as irregular dikes in drill cores. The thickness of X porphyry dikes in drill cores varies from several to tens of centimeters (Zhao et al. 2015) (Fig. 2B). The X porphyry has similar composition to the P porphyry except for a greater abundance of biotite phenocrysts. The X porphyry possesses unidirectional solidification textures (UST), intensive potassic alteration and weak propylitic alteration, but in general it is poorly mineralized (Yang et al. 2009). No direct cross-cutting relationships between the P and X porphyry has been documented previously, or observed in this study. However, previous studies assume it post-dates the P porphyry because it cuts barren potassic stage quartz veins in the Rongmucuola pluton (Yang et al. 2009; Zhao et al. 2015). The reported zircon LA-ICP-MS U-Pb age is identical, within uncertainty, to that of the P porphyry (15.9 ± 0.3 Ma) (Zhao et al. 2015).

Aplite

In addition to the P and X porphyry units, fracture controlled, thin (several to tens of cm wide) aplite dykes (Fig.3C and E) cross-cut the Rongmucuola pluton (Yang et al. 2009; Zhao et al. 2015). The aplite is widely distributed in drill cores but no cross-cutting relationship has been documented between the aplite and P or X porphyry. The aplite units are characterised by intergrowths of fine-grained (~1 mm) anhedral alkali feldspar and quartz (Yang et al. 2009; Zhao et al. 2015) with disseminated magnetite and pyrite throughout. The fine grained texture suggests that this aplite experienced rapid cooling and crystallized immediately after

emplacement (Webber et al. 1999). It has been assumed that the aplite is coeval or slightly older than the X porphyry as potassic stage irregular-planar quartz-K-feldspar veins truncate the aplite units (Yang et al. 2009). Further, this study has observed barren sinusoidal quartz veins within the mineralized aplite (documented below; Fig. 4A), which we interpret to have formed during the transition between the magmatic and hydrothermal stage. To date, no radiometric date has been reported for the aplite units.

Post-ore quartz diorite

Mineralization was cross cut by a quartz-diorite dyke. The dyke is tens of cm wide and 2-6 m in length. It hosts phenocrysts of ~0.5-1 cm diameter including plagioclase (~5 %), quartz (5 %) and hornlende (3 %) set within a matrix of plagioclase, hornblende, quartz and biotite (Fig. 3D). The quartz-diorite is typically fresh with only plagioclase phenocrysts exhibiting minor alteration to a low-temperature assemblage of calcite-chlorite-sericite (Fig. 3D) (Yang et al. 2009, 2015). This unit is the youngest intrusion recognized at Qulong and has a zircon SIMS U-Pb age of 15.3 ± 0.2 Ma (Zhao et al. 2015).

Hydrothermal breccia

In addition to the magmatic units mentioned above, a hydrothermal breccia associated with the formation of the porphyry mineralization is also documented at Qulong. The breccia exists as a pipe (~100 m in diameter) and cross cuts the Rongmucuola pluton, and likely contemporaneous with the emplacement of the P porphyry. The breccia is predominantly composed of clasts (<10 cm) from the Rongmucuola granodiorite pluton and P porphyry, which are cemented by aplite. These clasts are intensively altered and mineralized (Yang et al. 2009; Zhao et al. 2015). In certain cases, the breccia possesses intense silicification with hematite alteration, cemented by a clay mineral-dominated matrix (e.g. kaolinite, illite).

Hydrothermal alteration phases

Akin to porphyry copper deposits worldwide, Qulong has a clearly zoned mineralization and alteration pattern. The relative chronology of the alteration assemblage at Qulong is; a) veinlets associated with the magmatic-hydrothermal transition stage; b) potassic (K-feldspar, biotite) alteration stage; c) propylitic alteration (chloritization) assemblages, and d) phyllic alteration (sericite) phases. The alteration and mineralization phases at Qulong have been described by Yang et al. (2009) and Qin et al. (2014). Here we summarize these findings together with the observations of this study.

Magmatic-hydrothermal transition stage quartz veins

This study reports the first record of ~0.5 cm wide sinusoidal quartz veins at Qulong hosted within the aplite dyke (Fig. 4A). The veins bear K-feldspar rims (~1 mm wide) at both sides and have localised clusters of fine-grained (<0.3 mm) pyrite grains. These barren veins represent silica-saturated melts/fluid formed at the magmatic-hydrothermal transition stage before potassic alteration. This process is also represented by Unidirectional Solidification Textures (UST) hosted by the X porphyry (Yang et al. 2008a). The sinusoidal quartz veins and UST are taken to represent the magmatic-hydrothermal transition stage at Qulong.

Potassic alteration

Potassic stage alteration assemblages at Qulong include the barren biotite and quartz veins (generally 2 mm wide) (Fig. 4B), chalcopyrite and molybdenite bearing quartz veins with K-feldspar halos, and chalcopyrite-molybdenite bearing quartz veins with biotite-feldspar-quartz assemblages (Fig. 4C-F). Potassic alteration phases are concentrated around the P porphyry and predominantly hosted by the Rongmucuola pluton and P porphyry, but also occur in the Yeba Formation and X porphyry. Cu-Mo bearing veins with K-feldspar halos are

the main ore-bearing potassic alteration assemblages at Qulong. These veins generally have a width of 0.5-3 cm (Fig. 4D and E). The nature of potassic alteration is characterized by selective replacement of plagioclase to K-feldspar, and tends to be more extensive near the P porphyry where almost all plagioclase grains were replaced by sericite, kaolinite and illite. Veinlets containing biotite have been divided into three types: 1) vein fillings comprising coarse-grained biotite grains (0.1-0.4 mm); 2) yellow-brown coloured biotite alteration halos (generally < 0.1 mm in width) along irregular quartz or quartz-anhydrite veins; and 3) primary biotite grains replaced by secondary biotite in the Rongmucuola pluton (Yang et al. 2009). Potassic alteration is the main mineralization stage at Qulong and directly controls bulk Cu-Mo mineralization. A progressive increase in intensity of potassic alteration was documented in the Rongmucuola pluton from shallow to depth.

Propylitic alteration

Propylitic alteration is extensively developed at Qulong in both the Rongmucuola pluton and the Yeba Formation. The propylitic alteration is characterized by pervasive weak chloritization of the primary biotite and intensive replacement of plagioclase by epidote in the Rongmucuola pluton (Fig. 4G-I) and Yeba Formation, respectively. Propylitic alteration in the X porphyry is relatively weak. In the Rongmucuola pluton, biotite, hornblende and plagioclase have experienced different degrees of replacement by chlorite-dominated assemblages. In the Yeba Formation, epidote dominated (>60 vol%) alteration assemblages, with quartz, chlorite and K-feldspar, are found as irregular to planar veins (1-2 mm wide). Generally, sulfides (e.g. pyrite, chalcopyrite) associated with propylitic alteration are less abundant than in the potassic alteration stage (Yang et al. 2009). Anhydrite veins (pink, 1-3 mm in grain size and ~0.5-2 cm wide) along with molybdenite mineralization (with minor chalcopyrite) fill in reopened potassic stage K-feldspar veins (Fig. 4J). It is thought that these

sulfides (molybdenite + chalcopyrite) belong to the propylitic alteration stage given that the K-feldspar assemblages in these veins are partially replaced by late stage molybdenite and chlorite.

Phyllic and hypogene argillic alteration

Phyllic and hypogene argillic alteration phases are widely distributed and overprint early stage alteration assemblages at Qulong. Phyllic and argillic alteration phases are more intense in the P porphyry than that in the Rongmucuola pluton and the X porphyry. In most cases, the intensive phyllic and argillic alteration have overprinted all igneous textures in the P porphyry. Similar to the potassic alteration, a progressive enhancement of phyllic and argillic alterations has been documented from shallow to depth in the Rongmucuola pluton. The main mineral phases of the phyllic and argillic alteration assemblages are sericite, pyrite, anhydrite and clay minerals, and these are spatially associated with minor chalcopyrite and molybdenite. These phases are generally fine-grained (0.5-3 mm) and difficult to recognize in hand specimen, but occasionally include coarse-grained (0.5-1 cm) pyrite and anhydrite crystals (Fig. 4 K and L).

Samples and methods

Samples

Representative quartz veins from the magmatic-hydrothermal transition stage, potassic alteration, propylitic and phyllic alteration stages were selected to study fluid inclusions, which allow us to constrain the nature and evolution of the ore-forming fluid. All the samples were collected from drill cores at 10 to ~600 meters.

All the magmatic units at Qulong have been dated by previous studies, except the ore-bearing aplite. One ore-bearing aplite sample (Fig. 3C) was selected to conduct secondary ion

mass spectrometry (SIMS) zircon U-Pb geochronology. SIMS was also utilized to determine the oxygen isotope composition of the zircons in order to aid the understanding of the U-Pb data, as well as the nature of ore-forming fluids.

Six molybdenite bearing quartz veins utilized for fluid inclusion analysis were also targeted for Re-Os dating to further constrain the timing of sulfide mineralization. Samples were selected from the aplite with a weak potassic alteration of K-feldspar (313-145; Fig. 4C), the potassic alteration stage (313-460, 001-640; Fig. 4D and E), the potassic-propylitic transition (1605-334, Fig. 4J) and the phyllic stage (1605-155; 1605-33, Fig. 4K).

Microthermometry and laser Raman spectroscopy

Microthermometric analysis of vein quartz hosted fluid inclusions in doubly polished wafers was carried out at the Geofluids Research Laboratory, National University of Ireland, Galway, using a Linkam THMSG600 heating and freezing stage mounted on a Olympus transmitted light microscope. Synthetic fluid inclusion standards (pure CO_2 and pure water) were used (Baumgartner et al. 2014) at -56.6, 0, 10.2, and 374 °C to correct the accuracy of the stage. Measurements below 31.1 ^{o}C, the critical point of CO_2, are accurate to ±0.2 ^{o}C, and measurements above this temperature are accurate to ±1 ^{o}C. The volumetric fraction of phases in fluid inclusions was estimated at room temperature by reference to the volumetric chart of Roedder (1984). Bulk salinity was calculated from the final ice melting temperature, or halite dissolution temperature (Bodnar and Vityk 1994) for hypersaline fluid inclusions. Homogenization conditions and isochores of individual fluid inclusion assemblages (FIAs) have been calculated with HokieFlincs_H_2O-NaCl program based on fluid inclusion volumetric data (P-V-T-X) (Steele-MacInnis et al. 2012).

Solid and gas phases from selected fluid inclusions were identified using laser Raman spectroscopy (LRS) at the Geofluids Research Laboratory, National University of Ireland Galway. The LRS analysis was conducted on a Horiba Lab Ram II spectrometer equipped

316 with a 600 groove·mm^{-1} diffraction grating, confocal optics, a Peltier-cooled CCD detector
317 (255 by 1024 pixel array at -67 °C) and an Olympus BX41 microscope arranged in 180°
318 backscatter geometry. Sample excitation was achieved using a Ventus diode-pumped,
319 continuous wavelength, 532 nm laser with a maximum power output of 50 mW. Raman
320 analysis was carried out using a 100x objective lens resulting in a laser spot size of ~2 µm.
321 Excitation power at the sample typically ranged between 10 and 20 mW.
322
323 CL imaging and EDS mineral identification methods
324 CL imaging and mineral inclusion identification were conducted with a Hitachi SU-70
325 FEG SEM at the G., J., Russell electron microscopy facility at Durham University.
326 Cathodoluminescence (CL) imaging was carried out at a 10 kV accelerating voltage with a
327 beam current of 1.63 nA at 16.8 mm working distance. Secondary electron images were taken
328 under the same accelerating voltage and working distance but at a lower beam current (0.6
329 nA). Mineral inclusions were identified by EDS with 15 kV accelerating voltage and 0.93 nA
330 beam current at 15 mm working distance.
331
332 SIMS zircon oxygen isotope and U-Pb dating analytical method
333 Guided by CL images, zircon oxygen isotope analysis and U-Pb dating were carried out at
334 the Institute of Geology and Geophysics, Chinese Academy of Sciences with CAMECA
335 IMS-1280 SIMS and CAMECA IMS-1280HR SIMS, respectively. Sample preparation and
336 instrument operation conditions are the same as in Li et al. (2009, 2010a,b) and are briefly
337 summarized here. Zircon grains were mounted with zircon oxygen isotope standards (Penglai
338 zircon and Qinghu zircon) (Li et al. 2010b, 2013) and zircon geochronology standards
339 (Plešovice and Qinghu zircon) (Sláma et al. 2008; Li et al. 2013) and then polished and
340 coated with gold.

For O analysis, the Cs^+ primary ion beam was accelerated at 10 kV, with an intensity of ca. 2 nA and rastered over a 10 μm area. The spot size (ellipse) was about 10 × 20 μm in diameter. The normal incidence electron flood gun was used to compensate for sample charging during analysis with homogeneous electron density over a 100 μm oval area. A 60 eV energy window was used together with a mass resolution of ca. 2500. Oxygen isotopes were measured using multi-collection mode on two off-axis Faraday cups. The intensity of ^{16}O was typically 10^9 cps. The NMR (Nuclear Magnetic Resonance) probe was used for magnetic field control with stability better than 3 ppm over 16 h on mass ^{17}O. One analysis took ca. 5 min consisting of pre-sputtering (~120 s), automatic beam centering (~60 s) and integration of oxygen isotopes (20 cycles × 4 s, total 80 s). Uncertainties on individual analyses were usually better than 0.3-0.4 ‰ (2 SE). The instrumental mass fractionation factor (IMF) was corrected using Penglai zircon with a $\delta^{18}O$ value of 5.3 ‰ (Li et al. 2010b). Measured $^{18}O/^{16}O$ ratios were normalized by using V-SMOW compositions ($^{18}O/^{16}O$ = 0.0020052), and then corrected for the IMF. An in-house zircon standard (Qinghu) was used to ascertain the veracity of the IMF and 15 measurements of Qinghu zircon in this research yielded a weighted mean of 5.49 ± 0.37 ‰ (2 SD), which is consistent with the recommended value of 5.4 ± 0.2 ‰ (Li et al. 2013).

During U-Pb analysis, zircon grains were sputtered by an O_2^- primary ion beam with an intensity of ca. 8 nA and a diameter of 20 μm. An ellipsoidal spot approximately 20 × 30 μm in size was created at the sample surface as the ion beam was at an angle with the sample surface. U-Pb concentration and isotopic compositions were calibrated against the Plešovice zircon standard. Common Pb was corrected using measured non-radiogenic ^{204}Pb and an average present day crustal Pb compositions (Stacey and Kramers 1975). Concordia plot and ages are calculated by Isoplot 3.0 (Ludwig 2003). The quality of the data was assessed by analyzing the Qinghu zircon standard between samples. Five analyses of the Qinghu zircon standard during this study yielded a weighted average $^{206}Pb/^{238}U$ age of 160.1 ± 4.6 Ma (95 %

conf.), which is in good agreement with the reported reference value of 159.5 ± 0.2 Ma (Li et al. 2013).

Molybdenite Re-Os dating method

Molybdenite (0.3-2 mm) bearing quartz veins were crushed in an agate pestle to 5 mesh and then hand-picked under a microscope to remove non-molybdenite bearing phases. A known amount of material was placed into a Savillex Teflon digestion vessel with 8 ml of 32N HF (ROMIL Ltd. UpA high-purity HF) and left at room temperature for 24 hours (Lawley and Selby 2012). This digestion process was repeated until most of the quartz had been liberated. After this, the HF was removed by rinsing the material three times with MQ, followed by ethanol rinsing. The samples were then dried at 30 ºC. The material was further purified by traditional heavy liquid floating technology, and the estimated purity was better than 95 %.

The Re-Os analytical protocol follows that documented by Selby and Creaser (2001). In brief, a known amount molybdenite aliquant and spike solution (^{185}Re plus isotopically normal Os) was loaded into a Carius tube with 15.5 N HCl (3 ml) and 16 N HNO_3 (6 ml), sealed, and digested at 220 ºC for ~24 hours. Osmium was isolated from the acid medium using solvent extraction ($CHCl_3$) at room temperature and further purified by micro-distillation method. The rhenium fraction was separated by NaOH-acetone solvent extraction and standard anion column chromatography. Rhenium and osmium were loaded on to Ni and Pt filaments, respectively. The isotopic compositions were measured by negative thermal ionization mass spectrometry (N-TIMS) (Creaser et al. 1991). Analyses were conducted on a Thermo Scientific TRITON mass spectrometer, with Re and Os isotopic compositions measured using static Faraday collection mode. The Re and Os isotopic composition analytical uncertainties are propagated with spike calibrations, sample and spike weighting uncertainty, reproducibility of Re and Os isotope standard values, as well as blank

abundances and isotopic compositions. During the study, Re and Os blanks were 4 pg and 1 pg, respectively, with the $^{187}Os/^{188}Os$ of the blank being 0.25 ± 0.02. The molybenite Re-Os model age is calculated using the equation $t = \ln(^{187}Os/^{187}Re + 1)/\lambda$. All analytical uncertainties were propagated with, and without, the ^{187}Re decay constant uncertainty (Smoliar et al. 1996; Selby et al. 2007).

Fluid inclusion data

Classification strategy

The superimposition of multiple hydrothermal fluid pulses is a common phenomenon in hydrothermal ore deposits, and is particularly common in porphyry copper systems (Seedorff et al. 2005; Rusk et al. 2008; Richards 2011). As a result of the superimposition of hydrothermal events it is common to find in one crystal fluid inclusions that were trapped during different stages of mineralization and record very different physical and chemical compositions (Audetat et al. 1998). As such, to avoid ambiguous results and to investigate the primary ore-forming fluids nature, only primary and pseudosecondary fluid inclusions were analyzed.

Fluid inclusions and fluid inclusion assemblages (FIAs) (Goldstein and Reynolds 1994) are abundant in quartz veins from all alteration stages at Qulong and range in size from 1 to 30 μm in diameter (Fig. 5). The majority of fluid inclusions examined in this study have a diameter between 6 and 15 μm. Primary fluid inclusions are defined when they are confined to a single growth zone (Fig. 5A). However, given the fact that most of the quartz grains are anhedral and lack clear growth zonation under transmitted light microscope, like many porphyry copper deposits (Rusk et al. 2008), most fluid inclusions studied here are linearly distributed pseudosecondary fluid inclusions trapped during the healing of micron-sized intra-grain fractures/cracks (Fig. 5A-C). Secondary fluid inclusions (Fig. 5B), generally distributed along late stage fractures, have an unknown origin in relation to the mineralization (Fig. 5A)

and were avoided during this study. Homogenization temperatures (Th) of the fluid inclusions obtained during microthermometry are used to further confirm the classification of the FIAs, and generally consistent Th values were yielded from the same FIA as defined during the petrographic study (Goldstein and Reynolds 1994).

Based on phases observed at room temperature, five types of fluid inclusion assemblages have been defined. They are classified as: $LV_{0\text{-}25}$ (liquid-rich two-phase FIAs, Fig. 5F), $LV_{25\text{-}60}$ (liquid-vapor two-phase FIAs, Fig. 5E), $LV_{60\text{-}100}$ (vapor-rich two-phase FIAs, Fig. 5D and I), $LV_{H\pm OP}$ (halite bearing FIAs with or without opaque minerals, Fig. 5G and H) and LV_{OP} (opaque minerals bearing FIAs without halite presence, Fig. 5J and M) (L=liquid, V=vapor, subscript number = volume percentage of vapor in fluid inclusions, H ± OP = presence of halite and/or opaque minerals. e.g. $LV_{0\text{-}25}$ refers to two-phase fluid inclusions contain 0-25 vol% of vapor; LV_{OP} refers to fluid inclusions that contain opaque minerals without observed halite crystals). Halite in $LV_{H\pm OP}$ fluid inclusions was identified by its cubic shape and optical isotropy (Fig. 5G-J and L), with sylvite distinguished from halite by its sub-cubic form and lower relief. Halite is the dominant salt crystal. Anhydrite is also present in $LV_{H\pm OP}$ and LV_{OP} fluid inclusions, and is identified by its transparent anisotropic prisms (Fig. 5K and L) with a diagnostic Raman signal (Burke 2001). Hematite in $LV_{H\pm OP}$ and LV_{OP} fluid inclusions was easily recognized from its red colour, hexagonal shape and high reflection index (Fig. 5M). However, most of the opaque minerals in $LV_{H\pm OP}$ and LV_{OP} fluid inclusions were not identified due to their small size (<1 μm). In many cases a FIA comprises more than one type of fluid inclusions. In such cases the classification is defined by the main type of fluid inclusion in that FIA (Goldstein and Reynolds 1994).

$LV_{0\text{-}25}$ type fluid inclusions commonly display negative crystal shapes (Fig. 5F), but also exhibit rounded to irregular shapes. These inclusions occur in trails, as scattered groups and isolated individuals.

$LV_{25\text{-}60}$ type fluid inclusions are dominated by negative crystal shapes and also exhibit rounded shapes (Fig. 5E), they occur in trails, as randomly distributed clusters and as isolated individuals, which are similar to the $LV_{0\text{-}25}$ type fluid inclusions.

$LV_{60\text{-}100}$ type fluid inclusions share similar distribution patterns as the $LV_{0\text{-}25}$ and $LV_{25\text{-}60}$ type fluid inclusions (Fig. 5 D and I). However, the difference between this type and $LV_{0\text{-}25}$ and $LV_{25\text{-}60}$ inclusions is that $LV_{60\text{-}100}$ homogenize to both the vapor (~30 % of them) and liquid (~70 % of them) phase.

$LV_{H\pm OP}$ type fluid inclusions host one or more halite daughter minerals ± opaque minerals (Fig. 5G, H and L), with variable volume percentages of vapor. Halite is the most common daughter minerals, but sylvite and anhydrite (Fig. 5K, L) are also observed. This type of fluid inclusion is either isolated or occurs as randomly distributed clusters and often contains small (~1 μm) unidentified opaque daughter minerals (Fig. 5G, H, J, L).

LV_{OP} type fluid inclusions host opaque minerals and anhydrite, but no other identifiable daughter phases at room temperature (Fig. 5J and M). They contain 5-60 vol% vapor phases, with the majority containing 10-20 vol% vapor. These inclusions are generally distributed as random clusters or as isolated individuals, but also spatially associated with halite-bearing fluid inclusions (Fig. 5J). These fluid inclusions are generally secondary or of an unknown origin, and are not further discussed.

Distribution of FIAs in alteration phases

The sinusoidal quartz vein (Fig. 4A) from the magmatic-hydrothermal transition stage hosts pseudosecondary $LV_{25\text{-}60}$ inclusions defined FIA, which are spatially associated with $LV_{60\text{-}100}$ inclusions.

Quartz bearing assemblages with potassic alteration selvages host abundant halite bearing fluid inclusions ($LV_{H\pm OP}$) that define several primary and pseudosecondary FIAs, with one

FIA also possessing vapor-rich two-phase fluid inclusions (LV_{60-100}). Pseudosecondary LV_{60-100} FIAs and LV_{25-60} FIAs are also present.

Quartz bearing assemblages from the propylitic alteration stage host abundant pseudosecondary liquid-vapor two-phase fluid inclusions (LV_{25-60}) which define FIAs. Some of these FIAs also contain vapor-rich two-phase fluid inclusions (LV_{60-100}). Liquid-rich two-phase fluid inclusions (LV_{0-25}) are also present in these samples as FIAs.

Quartz-bearing assemblages from phyllic alteration stage host abundant pseudosecondary FIAs that contain liquid-rich two-phase fluid inclusions (LV_{0-25}). Pseudosecondary liquid-vapor two-phase fluid inclusions (LV_{25-60}) FIA are also present.

Microthermometry

The majority of fluid inclusions homogenize to liquid with subsequent dissolution of halite when present, except for LV_{60-100} type fluid inclusions, which 30 % of them homogenize to the vapor phase. A few halite bearing fluid inclusions also homogenize by halite dissolution. In most cases, the opaque minerals do not dissolve despite heating to 450-500 ^{o}C for 2-3 hours.

For the FIA bearing both LV_{25-60} and LV_{60-100} inclusions from a quartz vein representing the magmatic-hydrothermal transition stage (No.1 in Fig. 4A), the inclusions homogenize to liquid with Th of 340-360 ^{o}C and yield salinities of 2-6 wt. % NaCl equiv. (n = 18; Fig.6A).

All Th and salinity inclusion data for quartz bearing potassic alteration selvages are shown in Fig. 6B. One primary halite-bearing FIA ($LV_{H\pm OP}$, No. 2 in Fig. 6B) yield Th of 419-436 ^{o}C and salinities of 50-52 wt. % NaCl equiv. (n = 11). A pseudosecondary halite-bearing FIA ($LV_{H\pm OP}$, No.3) spatially associated with vapor-rich two-phase fluid inclusions (LV_{60-100}) yield identical Th (388-405 ^{o}C). The halite bearing fluid inclusions have salinities of 41-45 wt% NaCl equiv (n = 8), with the vapor-rich two-phase fluid inclusions homogenizing to vapor possessing lower salinities (4-7 wt% NaCl equiv., n=6). Two

pseudosecondary vapor-rich two-phase FIAs (No. 4 and 5) yield similar salinities (1-6 wt% NaCl equiv), but have different Th (385-400 and 360-370 °C; n = 12 and 13, respectively). Two liquid-vapor two-phase (LV_{60-100}) pseudosecondary FIAs (No. 6) yield similar Th (335-355 °C) and salinity (2-7 wt% NaCl equiv; n = 18).

All Th and salinity data for quartz veins bearing a propylitic alteration selvage are shown in Fig. 6C. Three pseudosecondary liquid-vapor two-phase (LV_{25-60}) FIAs (also include vapor-rich two-phase fluid inclusions, No. 7) yield identical Th (all homogenize to liquid) of 335-360 °C and salinities of 1-7 wt% NaCl equiv (n = 31). One pseudosecondary liquid-vapor two-phase FIA (No. 8) give similar salinity values (2-7 wt% NaCl equiv), but slightly lower Th (318-332 °C, n = 9). A further FIA (No. 9) comprising pseudosecondary liquid-rich two-phase fluid inclusions yield similar Th of 270-290 °C and show broadly similar salinities of 2-11 wt% NaCl equiv (n = 14).

The Th and salinity inclusion data for a quartz bearing phyllic alteration selvage are shown in Fig. 6D. In general, salinities are similar between FIAs (No. 10-12), and range between 1 and 9 wt% NaCl equiv. In contrast, Th values vary within the FIAs from 265 to 340 ˚C. One pseudosecondary liquid-rich two-phase FIA (No. 12) yielded Th of 265-290 °C and salinities of 1-8 wt% NaCl equiv (n = 13). Another pseudosecondary FIA (No. 11) yielded slightly higher Th (295-310 °C) and possesses similar salinities (3-9 wt% NaCl equiv. n = 12). A slightly higher Th (325-340 °C) is recorded by another pseudosecondary liquid-vapor two-phase FIA (No. 10), with salinities of 2-8 wt% NaCl equiv (n = 13).

Zircon U-Pb, O isotopes and mineral inclusions

SIMS zircon U-Pb and oxygen isotope data of the aplite

The zircon U-Pb and oxygen isotope data of the aplite are summarized in Table 2 and illustrated in Fig. 8 and 9, respectively. All analytical spots were located on areas with clear CL zonation, while sieve textured grains and mineral inclusions rich zones were avoided for

potential Pb loss (Fig. 7). The U-Pb analysis was conducted at the same position after oxygen isotope analysis. The 37 U-Pb analyses plot on or near the Wetherill concordia curve between 140 and 185 Ma (Fig. 8A). These data are divided into two groups based on their $^{206}Pb/^{238}U$ age distribution (Fig. 8B). The first group consists of $^{206}Pb/^{238}U$ age values that vary from 140.7 to 156.3 Ma (n = 4). The $^{206}Pb/^{238}U$ age values from the second group (n = 33) range from 165.2 to 184.7 Ma and show a bimodal distribution (Fig. 8C). No systematic age variations were observed between the core and rim.

The zircon $\delta^{18}O$ values range from 4.2 to 5.5 ‰, and show a positive skewed asymmetric distribution (Fig. 9). Notably, 18 analyses yield an average of 4.85 ± 0.23 ‰ (1 SD) which is lower than the recommended mantle value (5.3 ± 0.3 ‰) (Valley et al. 2005), with the remaining 12 analyses within the mantle value (average = 5.31 ± 0.12 ‰, 1 SD). There is no trend in the $\delta^{18}O$ values between the zircon core and rim. Further, there is also no correlation between the $^{206}Pb/^{238}U$ age data and the $\delta^{18}O$ values.

Zircon hosted mineral inclusions

The zircon grains from the aplite are characterized by sieve textures and host abundant mineral inclusions that are predominantly in the core of the grains (Fig. 10). In addition to rutile and xenotime, feldspar, quartz and fluorapatite are also frequently observed. Feldspar and quartz (15-40 um) generally coexist and cross cut the zircon grains.

Molybdenite Re-Os data

Re-Os data are reported at 2 sigma level uncertainty in Table 3 and are graphically presented in Fig. 11. The Re-Os data uncertainties are presented with full propagation of the analytical uncertainties without/with the ^{187}Re decay constant uncertainty. Rhenium concentrations of the molybdenite samples vary from 64 to 324 ppm. As the purity of molybdenite samples studied here is better than 95 %, the recorded rhenium concentration

variations relate directly to the abundance in the analyzed molybdenite sample. No relationship between rhenium concentration and age is observed. The Re-Os dates are in agreement with the relative chronology of the Qulong porphyry system; a) magmatic-hydrothermal transition, b) potassic alteration, c) propylitic alteration, and d) phyllic alteration (Fig. 11). Sample 313-145 from the aplite which hosts the sinusoidal quartz veins has a Re-Os model age of 16.10 ± 0.07 [0.08] Ma. Samples 313-460 and 001-640 with potassic selvages yield identical Re-Os dates of 16.11 ± 0.06 [0.08] Ma and 16.10 ± 0.07 [0.09] Ma, respectively. Sample 1605-334 with a propylitic selvage has a slightly younger date of 16.01 ± 0.06 [0.08] Ma. Two samples (1605-155 and 1605-33) with phyllic selvages yield further younger dates of 15.93 ± 0.06 [0.08] Ma and 15.88 ± 0.06 [0.08] Ma, respectively. As these samples are not cogenetic and indicate a resolvable timespan, no isochron or weighted average is presented.

Discussion

Geochronology of Qulong

A significant amount of geochronology data (U-Pb, Re-Os, Fig. 12) has been published in an attempt to constrain the timeframe of the magmatism and mineralization at Qulong. Published $^{206}Pb/^{238}U$ age data yield a weighted mean of 17.2 ± 0.9 Ma (LA-ICP-MS, N = 243, 1 SD) (Hu et al. 2015; Zhao et al. 2015) and 16.5 ± 1.1 Ma (SHRIMP, n = 38, 1 SD) (Li and Rui 2004; Wang et al. 2006) for the Rongmucuola pluton (Fig. 12). For the syn-ore P porphyry $^{206}Pb/^{238}U$ age data yield a weighted mean of 16.3 ± 0.5 Ma (LA-ICP-MS, n = 15, 1 SD) (Zhao et al. 2015) and 17.1 ± 1.0 Ma (SHRIMP, n = 13, 1 SD) (Hou et al. 2004). The zircon grains from the X porphyry have $^{206}Pb/^{238}U$ age data that yield a weighted average of 15.9 ± 0.5 Ma (LA-ICP-MS, n = 18, 1 SD) (Zhao et al. 2015). The post-ore diorite has zircon $^{206}Pb/^{238}U$ age data that yield a weighted mean of 15.7 ± 0.4 Ma (LA-ICP-MS; n = 21, 1 SD) (Yang et al. 2015) and 15.3 ± 0.3 Ma (SIMS; n = 17, 1 SD) (Zhao et al. 2015). Published Re-

573 Os molybdenite model ages via ICP-MS analysis constrain mineralization from 16.85 to
574 15.36 Ma, and have large uncertainties (0.19-1.94 Ma) (Meng et al. 2003; Zheng et al. 2004;
575 Li et al. 2005; Wang et al. 2006). The current U-Pb and Re-Os data set is suggestive of a
576 prolonged magmatic-hydrothermal evolution history at Qulong (>3 m.y, Fig.12). However,
577 the significance of these dates, in terms of magmatic-hydrothermal onset and demise, cannot
578 be truly given before the systematic difference between the methods (SHRIMP, LA-ICP-MS,
579 ICP-MS) and laboratories has been assessed (Von Quadt et al. 2011; Li et al. 2015;
580 Schaltegger et al. 2015). In this case, the weighted mean of the $^{206}Pb/^{238}U$ age for all the
581 zircon grains is certainly not a good estimation for the age of porphyry emplacement
582 (Schoene 2014). Further, the standard deviations associated with the analysis also cannot be
583 used to assess the magma evolution as there is no assessment for the variation which either
584 reflects geological processes or analytical uncertainties. As such estimating the timescale of
585 magmatism and mineralization at Qulong based on these data is impossible and further high-
586 precision geochronology study is needed (e.g., CA-ID-TIMS; (Chiaradia et al. 2013; Schoene
587 2014; Schaltegger et al. 2015)).

588 Given the observation that the aplite units intrude the Miocene Rongmucuola pluton (Fig.
589 3E) (Yang et al. 2009; Qin et al. 2014), and are truncated by quartz veins with potassic
590 selvages (Yang et al. 2009), there should be no doubt that it is coeval or slightly than
591 the syn-ore P porphyry. However, zircon SIMS $^{206}Pb/^{238}U$ age data from the aplite yield
592 concordant Jurassic ages (Fig. 8, 172-182 Ma). These zircon grains show clear zonation in
593 CL images (Fig. 7) without evidence of contamination from inherent cores, and no systematic
594 age variations between the core and the rim of the zircon grains. In addition, the concordia
595 data sets argue against Pb loss, thus we conclude that the Jurassic dates are not an analytical
596 manifestation or related to the disturbance of the U-Pb system, but in fact indicate there was
597 no zircon growth during the crystallization of the aplite (Bea et al. 2007).

598 The aplite has been previously suggested to be a quench product of the magma that also
599 produced the P porphyry (Yang et al. 2009). If this is the case, zircons with Jurassic cores
600 should also be observed in the P porphyry unless all the old, inherited grains have been
601 resorbed. As zircon is well known for its resistance in most geological conditions, plus the
602 lack of Jurassic cores documented in zircon grains from the P porphyry (Hou et al. 2015), the
603 aplite likely did not originate from the same magma as the P porphyry. A possible scenario is
604 the aplite represents rapid crystallization of a magma derived principally from melting of the
605 Jurassic igneous units (e.g., the Yeba Formation) during the emplacement of the Miocene
606 intrusions, e.g. during the emplacement of the P porphyry, and no Miocene zircon growth
607 during its crystallization (Bea et al. 2007).
608 Although there is no direct constraint for the emplacement age of the aplite, its minimum
609 crystallization age can be bracketed by a Re-Os age from molybdenite from the aplite unit
610 (16.11 ± 0.06 [0.08] Ma; sample 313-145; this study). Thus the aplite was formed before the
611 main potassic alteration-mineralization stage, and likely contemporaneous with the final
612 crystallization of the P porphyry, with the fluids of the sinusoidal quartz vein hosted by the
613 aplite recording the magmatic-hydrothermal transition (Lindsay et al. 1995).
614 The sieve textures and quartz-feldspar inclusions (Fig. 10) in the zircon grains of the
615 aplite suggest the aplite experienced extensive interaction with hydrothermal fluids, e.g., the
616 fluid associated with the sinusoidal quartz vein. The low $\delta^{18}O$ values (4.2-5.0 ‰, Table 2
617 and Fig. 9) from the aplite hosted zircon grains suggest these zircon are either crystallized
618 from low $\delta^{18}O$ magma (Wang et al. 2011), or experienced alteration by low $\delta^{18}O$ fluid
619 (Valley 2003). However, subduction related Jurassic magmatic rocks in the Gangdese
620 porphyry copper belt have $\delta^{18}O$ values of 5.5-7 ‰, so the low zircon $\delta^{18}O$ values may be best
621 explained by low $\delta^{18}O$ fluid alteration (Taylor 1968).
622 The Re-Os dates for molybdenite from quartz veins bearing potassic, propylitic and
623 phyllic selvages support the relative chronology of the hydrothermal evolution at Qulong (Fig.

11). Molybdenite in veins with potassic selvages yields identical Re-Os dates of 16.11 ± 0.06 [0.08] Ma and 16.10 ± 0.07 [0.09] Ma, with a slightly younger date (although overlapping within uncertainty) for the propylitic stage (16.01 ± 0.06 [0.08] Ma), and further younger ages for the phyllic stage (15.93 ± 0.06 [0.08] Ma and 15.88 ± 0.06 [0.08] Ma). To date, the Re-Os dates of this study provide the most robust timing constraints for the hydrothermal evolution at Qulong, suggesting a maximum duration of 350 kyr, which is much less than the uncertainties of the U-Pb (SHRIMP/LA-ICP-MS) dates for the P and X porphyry units, and the post-ore diorite.

A potential concern for an underestimation of the mineralization lifespan is that molybdenite may have formed entirely during the potassic phase, with some veins being overprinted by propylitic and phyllic alteration. However, no evidence of overprint/replacement of the molybdenite bearing veins was observed in this study. Furthermore, the argeement of the relative chronology shown by the alteration phases and the Re-Os molybdenite dates coupled with cessation of mineralization/hydrothermal activity represented by the 15.88 Ma phyllic assemblages in this study, and a 15.7 ± 0.2 Ma hydrothermal biotite Ar-Ar age (Zhao et al. 2015) agrue against a greater duration for hydrothermal activity.

Fluid compositions

The first ice-melting temperature for the majority of the two-phase aqueous fluid inclusions is < -23 ^{o}C, which indicates the presence of other chemical species besides NaCl and KCl (e.g. Ca, Fe and Mg) (Sterner and Bodnar 1984; Rusk et al. 2008). As anhydrite has been recognized throughout most of the alteration and mineralization assemblages (Zheng et al. 2004; Yang et al. 2009), and is present as daughter minerals in fluid inclusions (Fig. 5K and L), the fluid should be Ca-rich and oxidized (Xiao et al. 2012). Hematite is also a common opaque trapped mineral in the fluid inclusions (Fig. 5M). Therefore, it is reasonable

to assume that the fluid contains Na, K, Ca, Fe, Cu and Mo, with the anions Cl and S. As all of the fluid inclusions have first ice-melting temperatures > -60 ^{o}C, Br and Li are considered as insignificant in regards to the bulk composition of the hydrothermal fluids (Davis et al. 1990). CO_2 in LV_{25-60} fluid inclusions is identified by Laser Raman, butbut liquid CO2 was not observed at room temperature, nor clathrate formation was recorded in this study, thus only as a minor component (≤3.5 mol%) (Azbej et al. 2007).

The early K-feldspar halos show dissolution textures (e.g., sieve textures, Fig. 4D), with quartz phenocrysts in the P porphyry exhibiting diagnostic resorbed shapes with embayments (Fig. 3B) (Yang et al. 2009; Qin et al. 2014). This suggests that the hydrothermal fluid potentially contains corrosive acid, e.g. hydrofluoric acid (McPhie et al. 2011). Zircon grains from the aplite host abundant fluorapatite inclusions, together with the sieve textures related to hydrothermal alteration as demonstrated by low $\delta^{18}O$ values, are highly suggestive of the hypothesis that the hydrothermal fluid was fluorine rich. Similar quartz resorption textures have been recognized in Cu–Zn skarn at the Empire Mine, Idaho, and are attributed to high fluorine activities during the alteration and mineralization processes (Chang and Meinert 2004). In addition, fluorine-rich fluids have also been proposed to explain the formation of amoeboid clasts in the Olympic Dam IOCG deposit (McPhie et al. 2011). However, no fluorite has been recognized at Qulong (Zheng et al. 2004). This may either reflect a low fluorine concentration in the fluid or fluorite minerals were dissolved by later stage hydrothermal fluids.

Trapping conditions constraints and depth estimation

Determining the formation depth of a porphyry copper ore deposit is challenging, as such the depth of porphyry ore formation for many deposits is not precisely constrained (Seedorff et al. 2005; Rusk et al. 2008). Fluid inclusion studies, however, are widely used to help model ore-fluid trapping pressures and to estimate the formation depths.

Without independent pressure and temperature estimates, the halite-bearing FIA from the potassic alteration stage that are spatially associated with vapor-rich two-phase fluid inclusions (Fig. 5I, No. 3 in Fig. 6B) provides the best estimation for the conditions of ore formation at Qulong. This association suggests fluid boiling. Therefore, the homogenization temperatures (388-405 ^{o}C with an average of 398 ^{o}C) and homogenization pressure (250-290 bar, average of 270 bar) (Steele-MacInnis et al. 2012) of this specific FIA equals the trapping temperature and pressure, respectively. This trapping pressure suggests a formation depth of 1 km at lithostatic pressure or 2.7 km at hydrostatic pressure, given this sample has a current depth of 0.4 km, either 0.6 or 2.3 km erosion occurred following ore formation.

For the sinusoidal quartz vein that represents the magmatic-hydrothermal transition stage, the liquid-vapor two-phase FIA (No. 1) yields Th of 350 ^{o}C. Typical ductile-brittle transition in high level systems (e.g. porphyry copper deposits), which represents mechanical failure of a magma chamber and release of hydrothermal fluids occurs at temperatures < 425 ^{o}C (Landtwing et al. 2005; Richards 2011). If we consider 425 $^{\circ}$C as the uppermost trapping temperature for the FIA in the sinusoidal quartz vein, a ~0.7 kbar trapping pressure is determined (Fig. 13A). This pressure equals to ~2.7 km depth under lithostatic pressure and ~7 km under hydrostatic pressure. The lithostatic pressure inferred depth is consistent with the temporally later potassic alteration stage exhibiting boiling under hydrostatic pressure (No. 3, Fig. 13), this indicates that the sinusoidal vein was formed under lithostatic pressure.

Assuming trapping at hydrostatic conditions of 2.3-2.7 km depth for the rest of the FIAs, we present the best estimates for the trapping temperatures of fluids associated with potassic, propylitic and phyllic stages (Table 4). For potassic stage samples the pseudosecondary halite-bearing FIA yields average trapping temperature of 425 ^{o}C (No. 2, Fig. 13B). Two pseudosecondary vapor-rich two-phase FIAs yield average trapping temperature of 390 and 380 ^{o}C (No. 4 and 5, Fig. 13A). Two liquid-vapor two-phase pseudosecondary FIAs yield average trapping temperature of 360 ^{o}C (No. 6, Fig. 13A).

Three pseudosecondary liquid-vapor two-phase FIAs from the propylitic alteration stage yield trapping temperatures of 365 °C (No. 7, Fig. 13A), the pseudosecondary liquid-vapor two-phase FIA gives trapping temperature of 340 °C (No. 8, Fig. 13A), two pseudosecondary liquid-rich two-phase FIAs yield a trapping temperature of 290 °C (No. 9, Fig. 13A). For FIAs from the phyllic alteration stage, the pseudosecondary liquid-vapor two-phase fluid inclusions yield a trapping temperature of 345 °C (No. 10, Fig. 13A), while the pseudosecondary liquid-rich two-phase ones yield a trapping temperature of 310 and 285 °C (No. 11 and 12, Fig. 13A).

The fluid inclusion data presented here suggests the transition between lithostatic and hydrostatic pressure occurred at the initial stages of ore formation. The temperature at the magmatic-hydrothermal transition stage (425 °C) is significantly lower than that (573 predicted by Yang et al. (2009). This may suggest meteoric water involvement during the crystallization of the aplite, as indicated by the low $\delta^{18}O$ values recorded in zircons within the aplite. During the mineralization process, the fluid pressure remained broadly similar, with temperatures decreasing from potassic to phyllic stages. The very steady fluid pressure at hydrostatic conditions during the mineralization process indicates that the Qulong system experienced mechanical failure of the magma chamber before the mineralization processes, e.g. explosive pressure release marked by the breccia pipes (Fig. 2).

In addition, our data suggests a minimum ~2.3 km of erosion since the formation of Qulong. This amount of erosion is, however in contrast with current estimates that state there has been no significant regional uplift or erosion in central Tibet since the Miocene (Rowley and Currie 2006). Nevertheless, our fluid inclusion data, coupled with the absence of Miocene volcanism at Qulong, which is commonly observed in porphyry systems formed in extensional environments (Sillitoe 2010), is indicative of appreciable erosion in the Qulong area. Further, the exposure of several other Miocene porphyry systems near Qulong without

Miocene volcanic units (e.g., Jiama and Lakang'e; Fig. 1) may indicate that ~2 km of erosion is more widespread than previously considered.

Conclusion

Molybdenite Re-Os dating confirms that the bulk Cu and Mo mineralization at Qulong occurred between 16.10 ± 0.06 [0.08] Ma and 15.88 ± 0.06 [0.08] Ma (bracketed value is with ^{187}Re decay constant uncertainty). This timeframe is much less than the uncertainties of published U-Pb and Re-Os data. Though the published geochronology data seems to suggest a long-lived intrusive episode of the Miocene granodioritic to monzonitic rocks at Qulong, it is impossible to use the weighted mean and uncertainty to address the emplacement age and duration of magmatism until high-precision data is available (e.g. zircon CA-ID-TIMS).

The purely Jurassic aged zircons in the syn-ore aplite possessing a low oxygen isotope composition (4.85 ± 0.23 ‰), and sieve textures and mineral inclusions (quartz, feldspar and fluorapatite) indicate that the aplite is a remelt of Jurassic rocks which crystallized rapidly during the emplacement of the P porphyry, with involvement of meteoric fluid.

The ore-forming fluid contains Na, K, Ca, Fe, Cu and Mo, along with Cl and S. Fluorine is also an essential component as demonstrated by the presence of fluorapatite in zircon grains, as well as the dissolution textures of K-feldspar from the potassic stage and quartz phenocrysts in the P porphyry. Fluid inclusion study confirms the magmatic-hydrothermal transition occurred at ~425 ^{o}C under lithostatic pressure, while potassic, propylitic and phyllic alteration occurred at hydrostatic pressure with temperature progressively decreasing from 425 to 280 ^{o}C. The fluid inclusion data presented here suggest the Qulong porphyry system was formed at a paleo depth of ~2.7 km. This implies that ~2.3 km of erosion has occurred at Qulong after its formation, which may be related with regional uplift in the Lhasa terrane.

Acknowledgements

The authors thank You-Ye Zheng and Guang-Wu Jiang for access to Qulong. Jia Chang and Rui Wang assisted with the fieldwork. We would like to thank Jeremy Richards for his invaluable and constructive suggestions in clarifying various aspects regarding data presentation and interpretation. We appreciate Kate Horan, Massimo Chiaradia, Jing-Jing Zhu and Rui-Zhong Hu for their insightful comments that helped improve the presentation. YL received financial support from Durham University, China Scholarship Council, Society of Economic Geologists, International Association of Geochemistry, and the Geological Society of London. DS acknowledges the support of the TOTAL endowment fund.

762 **References**

763 Aitchison JC, Ali JR, Davis AM (2007) When and where did India and Asia collide? Journal of Geophysical
764 Research 112:1-19. doi: 10.1029/2006jb004706.

765 Ali JR, Aitchison JC (2008) Gondwana to Asia: Plate tectonics, paleogeography and the biological connectivity
766 of the Indian sub-continent from the Middle Jurassic through latest Eocene (166-35 Ma). Earth-Science
767 Reviews 88:145-166. doi: 10.1016/j.earscirev.2008.01.007.

768 Audetat A, Gunther D, Heinrich CA (1998) Formation of a magmatic-hydrothermal ore deposit: insights with
769 LA-ICP-MS analysis of fluid inclusions. Science 279:2091-2094. doi: 10.1126/science.279.5359.2091.

770 Azbej T, Severs MJ, Rusk BG, Bodnar RJ (2007) In situ quantitative analysis of individual H_2O-CO_2 fluid
771 inclusions by laser Raman spectroscopy. Chemical Geology 237:255-263. doi:
772 10.1016/j.chemgeo.2006.06.025.

773 Baumgartner M, Bakker RJ, Doppler G (2014) Re-equilibration of natural H2O-CO2-salt-rich fluid inclusions in
774 quartz-Part 1: experiments in pure water at constant pressures and differential pressures at 600 degrees
775 C. Contributions to Mineralogy and Petrology 168:1-14. doi: Artn 101710.1007/S00410-014-1017-3.

776 Bea F, Montero P, Gonzalez-Lodeiro F, Talavera C (2007) Zircon inheritance reveals exceptionally fast crustal
777 magma generation processes in central iberia during the cambro-ordovician. Journal of Petrology
778 48:2327-2339. doi: DOI 10.1093/petrology/egm061.

779 Bodnar RJ, Vityk MO (1994) Interpretation of microthermometric data for H_2O-NaCl fluid inclusions In:
780 Frezzotti BDVaML (ed) Fluid inclusions in minerals: Methods and applications. Virginia Tech,
781 Blacksburg, VA, pp 117-130.

782 Bodnar RJ, Lecumberri-Sanchez P, Moncada D, Steele-MacInnis M (2014) 13.5 - Fluid Inclusions in
783 Hydrothermal Ore Deposits In: Turekian HDHK (ed) Treatise on Geochemistry (Second Edition).
784 Elsevier, Oxford, pp 119-142.

785 Burke EAJ (2001) Raman microspectrometry of fluid inclusions. Lithos 55:139-158. doi: Doi 10.1016/S0024-
786 4937(00)00043-8.

787 Cathles LM, Erendi AHJ, Barrie T (1997) How long can a hydrothermal system be sustained by a single
788 intrusive event? Economic Geology 92:766-771. doi: 10.2113/gsecongeo.92.7-8.766.

789 Chang ZS, Meinert LD (2004) The magmatic-hydrothermal transition - evidence from quartz phenocryst
790 textures and endoskarn abundance in Cu-Zn skarns at the Empire Mine, Idaho, USA. Chemical
791 Geology 210:149-171. doi: 10.1016/j.chemgeo.2004.06.018.

792 Chiaradia M, Schaltegger U, Spikings R, Wotzlaw J-F, Ovtcharova M (2013) How Accurately Can We Date the
793 Duration of Magmatic-Hydrothermal Events in Porphyry Systems?—An Invited Paper. Economic
794 Geology 108:565-584.

795 Chiaradia M, Schaltegger U, Spikings R (2014) Time Scales of Mineral Systems-Advances in Understanding
796 Over the Past Decade. Soc Econ Geol Spec P:37-58.

797 Cooke DR, Hollings P, Walsh JL (2005) Giant porphyry deposits: Characteristics, distribution, and tectonic
798 controls. Economic Geology 100:801-818. doi: Doi 10.2113/100.5.801.

799 Cooke DR, Hollings P, Wilkinson JJ, Tosdal RM (2014) 13.14 - Geochemistry of Porphyry Deposits In:
800 Turekian HDHK (ed) Treatise on Geochemistry (Second Edition). Elsevier, Oxford, pp 357-381.

801 Creaser RA, Papanastassiou DA, Wasserburg GJ (1991) Negative Thermal Ion Mass-Spectrometry of Osmium,
802 Rhenium, and Iridium. Geochimica Et Cosmochimica Acta 55:397-401. doi: Doi 10.1016/0016-
803 7037(91)90427-7.

804 Davis DW, Lowenstein TK, Spencer RJ (1990) Melting Behavior of Fluid Inclusions in Laboratory-Grown
805 Halite Crystals in the Systems NaCl-H_2O, NaCl-KCl-H_2O, NaCl-$MgCl_2$-H_2O, and NaCl-$CaCl_2$-H_2O.
806 Geochimica Et Cosmochimica Acta 54:591-601. doi: Doi 10.1016/0016-7037(90)90355-O.

807 Goldstein RH, Reynolds TJ (1994) Systematics of fluid inclusions in diagenetic minerals. Society for
808 Sedimentary Geology, US.

809 Hou ZQ, Gao YF, Qu XM, Rui ZY, Mo XX (2004) Origin of adakitic intrusives generated during mid-Miocene
810 east-west extension in southern Tibet. Earth and Planetary Science Letters 220:139-155. doi:
811 10.1016/S0012-821x(04)00007-X.

812 Hou ZQ, Yang ZM, Qu XM, Meng XJ, Li ZQ, Beaudoin G, Rui ZY, Gao YF, Zaw K (2009) The Miocene
813 Gangdese porphyry copper belt generated during post-collisional extension in the Tibetan Orogen. Ore
814 Geology Reviews 36:25-51. doi: 10.1016/j.oregeorev.2008.09.006.

815 Hou ZQ, Yang ZM, Lu YJ, Kemp A, Zheng YC, Li QY, Tang JX, Yang ZS, Duan LF (2015) A genetic linkage
816 between subduction- and collision-related porphyry Cu deposits in continental collision zones. Geology
817 43:247-250. doi: 10.1130/G36362.1.

818 Hu YB, Liu JQ, Ling MX, Ding W, Liu Y, Zartman RE, Ma XF, Liu DY, Zhang CC, Sun SJ, Zhang LP, Wu K,
819 Sun WD (2015) The formation of Qulong adakites and their relationship with porphyry copper deposit:
820 Geochemical constraints. Lithos 220:60-80. doi: 10.1016/j.lithos.2014.12.025.

821 Landtwing MR, Pettke T, Halter WE, Heinrich CA, Redmond PB, Einaudi MT, Kunze K (2005) Copper
822 deposition during quartz dissolution by cooling magmatic-hydrothermal fluids: The Bingham porphyry.
823 Earth and Planetary Science Letters 235:229-243. doi: 10.1016/j.epsl.2005.02.046.

824 Lawley CJM, Selby D (2012) Re-Os Geochronology of Quartz-Enclosed Ultrafine Molybdenite: Implications
825 for Ore Geochronology. Economic Geology 107:1499-1505.

826 Li GM, Rui ZY (2004) Diagenetic and Mineralization ages for the porphyry copper deposits in the Gangdise
827 Metallogenic Belt, Southern Xizang. Geotectonica et Metallogenia 28:165-170 (In Chinese with
828 English Abstract).

829 Li GM, Liu B, Qu WJ, Lin FC, Yu HQ, Feng CY (2005) The porphyry- skarn ore- forming system in Gangdese
830 Metallogenic Belt, southern Xizang: Evidence from molybdenite Re-Os age of porphyry- type copper
831 deposits and skarn- type copper polymetallic deposits. Geotectonica et Metallogenia 29:482-490 (In
832 Chinese with English Abstract).

833 Li XH, Liu Y, Li QL, Guo CH, Chamberlain KR (2009) Precise determination of Phanerozoic zircon Pb/Pb age
834 by multicollector SIMS without external standardization. Geochemistry, Geophysics, Geosystems
835 10:1-21. doi: 10.1029/2009gc002400.

836 Li XH, Li WX, Li QL, Wang XC, Liu Y, Yang YH (2010a) Petrogenesis and tectonic significance of the similar
837 to 850 Ma Gangbian alkaline complex in South China: Evidence from in situ zircon U-Pb dating, Hf-O
838 isotopes and whole-rock geochemistry. Lithos 114:1-15. doi: 10.1016/j.lithos.2009.07.011.

839 Li XH, Long WG, Li QL, Liu Y, Zheng YF, Yang YH, Chamberlain KR, Wan DF, Guo CH, Wang XC, Tao H
840 (2010b) Penglai Zircon Megacrysts: A Potential New Working Reference Material for Microbeam
841 Determination of Hf-O Isotopes and U-Pb Age. Geostandards and Geoanalytical Research 34:117-134.
842 doi: 10.1111/j.1751-908X.2010.00036.x.

843 Li XH, Tang GQ, Gong B, Yang YH, Hou KJ, Hu ZC, Li QL, Liu Y, Li WX (2013) Qinghu zircon: A working
844 reference for microbeam analysis of U-Pb age and Hf and O isotopes. Chinese Science Bulletin
845 58:4647-4654. doi: 10.1007/s11434-013-5932-x.

846 Li XH, Liu XM, Liu YS, Su L, Sun WD, Huang HQ, Yi K (2015) Accuracy of LA-ICPMS zircon U-Pb age
847 determination: An inter-laboratory comparison. Sci China Earth Sci 58:1722-1730. doi:
848 10.1007/s11430-015-5110-x.

849 Lindsay DD, Zentilli M, Rivera JRDL (1995) Evolution of an Active Ductile to Brittle Shear System
850 Controlling Mineralization at the Chuquicamata Porphyry Copper Deposit, Northern Chile.
851 International Geology Review 37:945-958. doi: 10.1080/00206819509465434.

852 Ludwig KR (2003) User's manual for Isoplot 3.00: a geochronological toolkit for Microsoft Excel. Kenneth R.
853 Ludwig.

854 McPhie J, Kamenetsky V, Allen S, Ehrig K, Agangi A, Bath A (2011) The fluorine link between a supergiant
855 ore deposit and a silicic large igneous province. Geology 39:1003-1006. doi: 10.1130/G32205.1.

856 Meng XJ, Hou ZQ, Gao YF, Huang W, Qu XM, Qu WJ (2003) Re-Os dating for molybdenite from Qulong
857 porphyry copper deposit in Gangdese metallogenic Belt, Xizangand its metallogenic significance.
858 Geological Review 49:660-666 (In Chinese with English Abstract).

859 Mercer CN, Reed MH, Mercer CM (2015) Time Scales of Porphyry Cu Deposit Formation: Insights from
860 Titanium Diffusion in Quartz. Economic Geology 110:587-602.

861 Qin KZ, Xia DX, Li GM, Xiao B, Duo J, Jiang GW, Zhao JX (2014) Qulong Porphyry-Skarn Cu-Mo Deposit,
862 Tibet. Science Press, Beijing (In Chinese).

863 Richards JP (2009) Postsubduction porphyry Cu-Au and epithermal Au deposits: Products of remelting of
864 subduction-modified lithosphere. Geology 37:247-250. doi: 10.1130/G25451a.1.

865 Richards JP (2011) Magmatic to hydrothermal metal fluxes in convergent and collided margins. Ore Geology
866 Reviews 40:1-26. doi: 10.1016/j.oregeorev.2011.05.006.

867 Richards JP (2013) Giant ore deposits formed by optimal alignments and combinations of geological processes.
868 Nature Geoscience 6:911-916. doi: 10.1038/NGEO1920.

869 Roedder E (1984) Fluid Inclusions. Mineralogical Society of America, US.

870 Rowley DB (1996) Age of initiation of collision between India and Asia: A review of stratigraphic data. Earth
871 and Planetary Science Letters 145:1-13. doi: Doi 10.1016/S0012-821x(96)00201-4.

872 Rowley DB, Currie BS (2006) Palaeo-altimetry of the late Eocene to Miocene Lunpola basin, central Tibet.
873 Nature 439:677-681. doi: 10.1038/nature04506.

874 Rusk BG, Reed MH, Dilles JH (2008) Fluid inclusion evidence for magmatic-hydrothermal fluid evolution in
875 the porphyry copper-molybdenum deposit at Butte, Montana. Economic Geology 103:307-334. doi:
876 DOI 10.2113/gsecongeo.103.2.307.

877 Samson I, Anderson A, Marshall D (2003) Fluid inclusions: analysis and interpretation. Mineralogical
878 Association of Canada, Canada.

879 Schaltegger U, Schmitt AK, Horstwood MSA (2015) U-Th-Pb zircon geochronology by ID-TIMS, SIMS, and
880 laser ablation ICP-MS: Recipes, interpretations, and opportunities. Chemical Geology 402:89-110. doi:
881 10.1016/j.chemgeo.2015.02.028.

882 Schoene B (2014) 4.10 - U–Th–Pb Geochronology In: Turekian HDHK (ed) Treatise on Geochemistry (Second
883 Edition). Elsevier, Oxford, pp 341-378.

884 Seedorff E, Dilles J, Proffett J, Einaudi M, Zurcher L, Stavast W, Johnson D, Barton M (2005) Porphyry
885 deposits: characteristics and origin of hypogene features. Economic Geology 100th Anniversary
886 Volume 29:251-298.

887 Selby D, Creaser RA (2001) Re-Os geochronology and systematics in molybdenite from the Endako porphyry
888 molybdenum deposit, British Columbia, Canada. Economic Geology and the Bulletin of the Society of
889 Economic Geologists 96:197-204. doi: Doi 10.2113/96.1.197.

890 Selby D, Creaser RA, Stein HJ, Markey RJ, Hannah JL (2007) Assessment of the ^{187}Re decay constant by cross
891 calibration of Re-Os molybdenite and U-Pb zircon chronometers in magmatic ore systems. Geochimica
892 Et Cosmochimica Acta 71:1999-2013. doi: 10.1016/j.gca.2007.01.008.

893 Sillitoe RH (2010) Porphyry Copper Systems. Economic Geology 105:3-41.

894 Sillitoe RH, Mortensen JK (2010) Longevity of Porphyry Copper Formation at Quellaveco, Peru. Economic
895 Geology 105:1157-1162. doi: DOI 10.2113/econgeo.105.6.1157.

896 Simmons SF, Brown KL (2006) Gold in magmatic hydrothermal solutions and the rapid formation of a giant ore
897 deposit. Science 314:288-291. doi: 10.1126/science.1132866.

Simmons SF, Brown KL (2007) The flux of gold and related metals through a volcanic arc, Taupo Volcanic Zone, New Zealand. Geology 35:1099-1102. doi: 10.1130/G24022a.1.

Sláma J, Košler J, Condon DJ, Crowley JL, Gerdes A, Hanchar JM, Horstwood MS, Morris GA, Nasdala L, Norberg N (2008) Plešovice zircon—a new natural reference material for U–Pb and Hf isotopic microanalysis. Chemical Geology 249:1-35.

Smoliar MI, Walker RJ, Morgan JW (1996) Re-Os ages of group IIA, IIIA, IVA, and IVB iron meteorites. Science 271:1099-1102. doi: DOI 10.1126/science.271.5252.1099.

Spencer ET, Wilkinson JJ, Creaser RA, Seguel J (2015) The Distribution and Timing of Molybdenite Mineralization at the El Teniente Cu-Mo Porphyry Deposit, Chile. Economic Geology 110:387-421. doi: 10.2113/econgeo.110.2.387.

Stacey Jt, Kramers J (1975) Approximation of terrestrial lead isotope evolution by a two-stage model. Earth and Planetary Science Letters 26:207-221.

Steele-MacInnis M, Lecumberri-Sanchez P, Bodnar RJ (2012) HOKIEFLINCS_H_2O-NaCl: A Microsoft Excel spreadsheet for interpreting microthermometric data from fluid inclusions based on the PVTX properties of H_2O-NaCl. Computers & Geosciences 49:334-337. doi: 10.1016/j.cageo.2012.01.022.

Sterner SM, Bodnar RJ (1984) Synthetic fluid inclusions in natural quartz I. Compositional types synthesized and applications to experimental geochemistry. Geochimica et Cosmochimica Acta 48:2659-2668.

Taylor Jr HP (1968) The oxygen isotope geochemistry of igneous rocks. Contributions to Mineralogy and Petrology 19:1-71.

Valley JW (2003) Oxygen isotopes in zircon. Zircon 53:343-385. doi: Doi 10.2113/0530343.

Valley JW, Lackey JS, Cavosie AJ, Clechenko CC, Spicuzza MJ, Basei MAS, Bindeman IN, Ferreira VP, Sial AN, King EM, Peck WH, Sinha AK, Wei CS (2005) 4.4 billion years of crustal maturation: oxygen isotope ratios of magmatic zircon. Contributions to Mineralogy and Petrology 150:561-580. doi: 10.1007/s0 Landtwing 0410-005-0025-8.

Van Hinsbergen DJ, Lippert PC, Dupont-Nivet G, McQuarrie N, Doubrovine PV, Spakman W, Torsvik TH (2012) Greater India Basin hypothesis and a two-stage Cenozoic collision between India and Asia. Proceedings of the National Academy of Sciences 109:7659-7664.

Von Quadt A, Erni M, Martinek K, Moll M, Peytcheva I, Heinrich CA (2011) Zircon crystallization and the lifetimes of ore-forming magmatic-hydrothermal systems. Geology 39:731-734.

Wang LL, Mo XX, Li B, Dong GC, Zhao ZD (2006) Geochronology and geochemistry of the ore-bearing porphyry in Qulong Cu (Mo) ore deposit, Tibet. Acta Petrologica Sinica 22:1001-1008 (In Chinese with English Abstract).

930 Wang R, Richards JP, Hou ZQ, Yang ZM (2014a) Extent of underthrusting of the Indian plate beneath Tibet
931 controlled the distribution of Miocene porphyry Cu-Mo ± Au deposits. Mineralium Deposita 49:165-
932 173. doi: 10.1007/s00126-013-0507-y.

933 Wang R, Richards JP, Hou ZQ, Yang ZM, Gu ZB, DuFrane SA (2014b) Increasing Magmatic Oxidation State
934 from Paleocene to Miocene in the Eastern Gangdese Belt, Tibet: Implication for Collision-Related
935 Porphyry Cu-Mo ± Au Mineralization. Economic Geology 109:1943-1965.

936 Wang R, Richards JP, Zhou L-m, Hou Z-q, Stern RA, Creaser RA, Zhu J-j (2015) The role of Indian and
937 Tibetan lithosphere in spatial distribution of Cenozoic magmatism and porphyry Cu–Mo deposits in the
938 Gangdese belt, southern Tibet. Earth-Science Reviews 150:68-94. doi: 10.1016/j.earscirev.2015.07.003.

939 Wang XC, Li ZX, Li XH, Li QL, Tang GQ, Zhang QR, Liu Y (2011) Nonglacial origin for low-δ18O
940 Neoproterozoic magmas in the South China Block: Evidence from new in-situ oxygen isotope analyses
941 using SIMS. Geology 39:735-738.

942 Webber KL, Simmons WB, Falster AU, Foord EE (1999) Cooling rates and crystallization dynamics of shallow
943 level pegmatite-aplite dikes, San Diego County, California. American Mineralogist 84:708-717.

944 Weis P, Driesner T, Heinrich CA (2012) Porphyry-copper ore shells form at stable pressure-temperature fronts
945 within dynamic fluid plumes. Science 338:1613-1616. doi: 10.1126/science.1225009.

946 Wilkinson JJ (2001) Fluid inclusions in hydrothermal ore deposits. Lithos 55:229-272. doi: Doi 10.1016/S0024-
947 4937(00)00047-5.

948 Xiao B, Qin KZ, Li GM, Li JX, Xia DX, Chen L, Zhao JX (2012) Highly Oxidized Magma and Fluid Evolution
949 of Miocene Qulong Giant Porphyry Cu-Mo Deposit, Southern Tibet, China. Resource Geology 62:4-18.
950 doi: 10.1111/j.1751-3928.2011.00177.x.

951 Yang ZM, Hou ZQ, Li ZQ, Song YC, Xie YL (2008a) Direct record of primary fluid exsolved from magma:
952 Evidence from unidirectional solidification texture (UST) in quartz found in Qulong porphyry copper
953 deposit, Tibet. Mineral Deposits 27:188-199 (In Chinese with English Abstract).

954 Yang ZM, Hou ZQ, Xia DX, Song YC, Li Z (2008b) Relationship between Western Porphyry and
955 mineralization in Qulong copper deposit of Tibet and its enlightenment to further exploration. Mineral
956 Deposits 27:28-36 (In Chinese with English Abstract).

957 Yang ZM, Hou ZM (2009) Genesis of Giant Porphyry Cu Deposit at Qulong, Tibet: Constrains from Fluid
958 Inclusions and H-O Isotopes. Acta Geologica Sinica 83:1838-1859 (In Chinese with English Abstract).

959 Yang ZM, Hou ZQ, White NC, Chang ZS, Li ZQ, Song YC (2009) Geology of the post-collisional porphyry
960 copper-molybdenum deposit at Qulong, Tibet. Ore Geology Reviews 36:133-159. doi:
961 10.1016/j.oregeorev.2009.03.003.

962 Yang ZM, Lu YJ, Hou ZQ, Chang ZS (2015) High-Mg Diorite from Qulong in Southern Tibet: Implications for
963 the Genesis of Adakite-like Intrusions and Associated Porphyry Cu Deposits in Collisional Orogens.
964 Journal of Petrology 56:227-253. doi: 10.1093/petrology/egu076.

965 Zhang ZM, Dong X, Santosh M, Zhao GC (2014) Metamorphism and tectonic evolution of the Lhasa terrane,
966 Central Tibet. Gondwana Research 25:170-189. doi: 10.1016/j.gr.2012.08.024.

967 Zhao JX, Qin KZ, Xiao B, McInnes B, Li GM, Evans N, Cao MJ, Li JX (2015) Thermal history of the giant
968 Qulong Cu–Mo deposit, Gangdese metallogenic belt, Tibet: Constraints on magmatic–hydrothermal
969 evolution and exhumation. Gondwana Research. doi: 10.1016/j.gr.2015.07.005.

970 Zheng YY, Xue YX, Cheng LJ, Fan ZH, Gao SB (2004) Finding,Characteristics and Significances of Qulong
971 Superlarge Porphyry Copper (Molybdenum) Deposit, Tibet. Earth Sciences 29:103-108 (In Chinese
972 with English Abstract).

973 Zhu DC, Zhao ZD, Niu YL, Dilek Y, Mo XX (2011a) Lhasa terrane in southern Tibet came from Australia.
974 Geology 39:727-730. doi: 10.1130/G31895.1.

975 Zhu DC, Zhao ZD, Niu YL, Mo XX, Chung SL, Hou ZQ, Wang LQ, Wu FY (2011b) The Lhasa Terrane:
976 Record of a microcontinent and its histories of drift and growth. Earth and Planetary Science Letters
977 301:241-255. doi: 10.1016/j.epsl.2010.11.005.

978 Zimmerman A, Stein HJ, Morgan JW, Markey RJ, Watanabe Y (2014) Re–Os geochronology of the El Salvador
979 porphyry Cu–Mo deposit, Chile: Tracking analytical improvements in accuracy and precision over the
980 past decade. Geochimica et Cosmochimica Acta 131:13-32. doi: 10.1016/j.gca.2014.01.016.

981

982

983

Figures and Tables

Fig. 1. Tectonic setting and geological map of the Gangdese Porphyry Copper Belt, Modified from Yang et al. (2009).

Fig. 2**.** Geological map (A) of the Qulong Cu-Mo porphyry deposit with cross sections (B), simplified and revised from Zhao et al. (2015).

Fig. 3. Representative images of the geology of the Qulong porphyry Cu-Mo deposit. A) Rongmucuola granodiorite pluton, (B) P porphyry, (C) aplite, (D) post-ore quartz-diorite, and (E) cross-cutting relationship between aplite and the Rongmucuola pluton. See text for detail.

Fig. 4. Photos showing alteration and mineralization characteristics of the Qulong porphyry Cu-Mo deposit. (A) Earliest A vein; (B) Early barren quartz vein and biotite vein; (C) Molybdenite vein hosted by aplite; (D) Main stage Cu-Mo veins with K-feldspar and biotite halos; (E, F, G) Cu-Mo mineralization with K-feldspar halos from the potassic-propylitic alteration stage; (H, I) Mo-Cu veins from the propylitic alteration stage; (J) Anhydrite veins with Cu-Mo halos from the phyllic alteration stage; (K) Pyrite-anhydrite vein from the phyllic alteration stage; (L) Argillic alteration sample. See text for detail.

Fig. 5. Distribution and characteristic features of fluid inclusions at Qulong. (A) Distribution of primary, pseudosecondary and origin unknown fluid inclusions; (B) Secondary fluid inclusions within late-stage fracture and pseudosecondary fluid inclusions; (C) Linear distributed pseudosecondary fluid inclusions; (D) Vapor rich two-phase FIA; (E) Liquid-vapor two-phase FIA; (F) Liquid-rich two-phase FIA; (G) Halite bearing FIA with/without opaque; (H) Halite-bearing FIA with/without opaque; (I) Vapor rich two-phase FIA; (J) Two-phase FIA spatially associated with halite-bearing fluid inclusions; (K) Anhydrite bearing fluid inclusion; (L) Halite bearing fluid inclusion with anhydrite and opaque minerals; (M) Opaque mineral and hematite bearing fluid inclusions without halite.

Fig. 6. Th-salinity plots of fluid inclusions from the magmatic-hydrothermal transition stage (A), potassic stage (B), propylitic stage (C) and phyllic stage (D). The ages quoted in the figures are from quartz-enclosed molybdenite Re-Os dates obtained in this study (Table 3). Numbers in blue indicate the FIA number discussed in the text.

Fig. 7. CL images of zircon grains from aplite sample, with SIMS locations, and U-Pb and O isotope data. Blue numbers indicate the zircon grain number noted in the first column of Table 2.

Fig. 8. (A) Concordia plot of the aplite zircon SIMS U-Pb data, (B) weighted average $^{206}Pb/^{238}U$ age plot, and (C) histogram showing a bimodal distribution of the $^{206}Pb/^{238}U$ ages. Note the calculated weighted average data in Fig. 8C does not represent geological meaningful ages, but indicates the source of the magma. See text for discussion.

Fig. 9. Histogram of aplite zircon SIMS oxygen isotope data, with mantle zircon values from Valley et al. (2005). See text for discussion.

Fig. 10. Secondary electron image showing the type and distribution of mineral inclusions in zircon grains from the aplite sample.

Fig. 11. Molybdenite Re-Os dates obtained for quartz veins bearing potassic, propylitic and phyllic selvages.

Fig. 12. A compilation of all published zircon U-Pb (LA-ICP-MS, SHRIMP, SIMS) and molybdenite Re-Os (ICP-MS) data of the Miocene units and mineralization at Qulong. Also shown are the Re-Os dates obtained in this study. Our SIMS U-Pb zircons dates for the aplite are not shown as they are all Jurassic. See text for data sources and discussion.

Fig. 13. Trapping pressure and temperature of hydrothermal fluids at Qulong associated with the magmatic-hydrothermal transition, potassic, propylitic and phyllic alteration and mineralization; (A) Isochores for a 5 wt% NaCl equiv, and (B) 40 wt% NaCl equiv NaCl-H_2O system (Samson et al. 2003). Hydrostatic and lithostatic pressures are calculated based on a density of 1 and 2.6 g/cm^3, respectively. Numbers at coloured star symbol indicate the FIA number discussed in the text. (C) Fluid pressure-temperature evolution of Qulong.

1046 Table 1. Geological summary for all magmatic units in the Qulong deposit including published ages.

Units	Distribution	Composition	Alteration and mineralization	Age (Mineral, method and data)
Yeba Formation	E-W direction in South Gangdese belt.	Andesitic crystal tuff, ignimbrite, and dacite; laminated slate, with interbedded sandstone and limestone; andesitic lava and volcanoclastic rocks.	Weak propylitic alteration, no mineralization except pyrite veins.	Zircon, LA-ICPMS U-Pb, 166.0 ± 1.8 Ma (Zhao et al. 2015).
Jurassic intrusions	Mid-western of Qulong	Dacite-rhyolite and rhyolite porphyry. quartz (20-25 vol%) and feldspar (8-10 vol%) as phenocrysts, with quartz and K-feldspar and biotite as groundmass.	Propylitic and phyllic alterations with abundant fracture controlled pyrite veins.	Zircon, SHRIMP U-Pb, 182.3 ± 1.5 Ma (Yang et al. 2009); Zircon, LA-ICPMS U-Pb, 160.7 ± 2.0 Ma (Zhao et al. 2015).
Rongmucuola pluton	East part of Qulong	Medium-coarse, hypidiomorphic-granular granodiorite. Coarse-grained (5-10 mm) plagioclase (30-40 vol%), K-feldspar (20-30 vol%), and medium grained (2-5 mm) quartz (15-20 vol%) and biotite (10-15 vol%), accessory minerals include apatite, magnetite, zircon, rutile.	Weak propylitic alteration, generally barren.	Zircon, LA-ICPMS U-Pb, 17.6 ± 0.3 Ma (Zhao et al. 2015).
	Central Qulong	Weakly porphyritic monzogranite. Coarse-grained (5-10 mm) plagioclase (30-40 vol%), K-feldspar (20-30 vol%), and medium grained (2-5 mm) quartz (15-20 vol%) and biotite (10-15 vol%), accessory minerals include apatite, magnetite, zircon, rutile.	Intensive potassic, propylitic and phyllic alteration and hosts the majority of the Cu-Mo in Qulong.	Zircon, LA-ICPMS U-Pb, 17.4 ± 0.4 Ma (Zhao et al. 2015).
P porphyry	Central Qulong	Coarse-grained monzogranite. Coarse-grained (3-8 mm) plagioclase (10-20 vol%), quartz (5-1- vol%) and K-feldspar (~5 vol%) as phenocrysts, the groundmass is dominated by quartz and feldspar.	Intensive potassic, propylitic and phyllic alteration and has been presumed as the ore-genitor porphyry.	Zircon, LA-ICPMS U-Pb, 16.2 ± 0.3 Ma (Zhao et al. 2015).
X porphyry	Central Qulong and drill cores	Coarse-grained biotite monzogranite. Mineralogy similar as P porphyry but contains more quartz.	Intensive potassic, weak propylitic and phyllic alteration, weak mineralized.	Zircon, LA-ICPMS U-Pb, 15.9 ± 0.3 Ma (Zhao et al. 2015).
Aplite	Central Qulong and drill cores	fine grained aplite Intergrowths of fine-grained (~1 mm) anhedral alkali feldspar and quartz.	Intensive potassic, weak propylitic and phyllic alteration, generally not mineralized.	No data reported
Quartz diorite dike	Mainly in drill cores	Quartz diorite dike Coarse phenocrysts (~0.5-1cm) of plagioclase (~5%), quartz (5%) and hornblende (3%) with a matrix comprise plagioclase and hornblende as well as quartz and biotite.	Weak phyllic alteration, post-mineralization thus barren.	Zircon, LA-ICPMS U-Pb, 15.3 ± 0.3 Ma (Zhao et al. 2015).

1047 Table 2. Zircon SIMS U-Pb and oxygen isotope data for the aplite sample.

1048

No	U ppm	Th ppm	Th/U	f_{206} %	$^{207}Pb/^{206}Pb$	±1σ %	$^{207}Pb/^{235}U$	±1σ %	$^{206}Pb/^{238}U$	±1σ %	rho	$t_{207/235}$ Ma	±1σ abs	$t_{206/238}$ Ma	±1σ abs	$\delta^{18}O$	±2σ abs
1	641	489	0.76	1.2	0.04044	3.59	0.15434	3.90	0.02768	1.52	0.39	145.7	5.3	176.0	2.6	5.5	0.25
2	972	1146	1.18	0.3	0.04799	1.48	0.18251	2.15	0.02758	1.56	0.72	170.2	3.4	175.4	2.7	5.1	0.21
3	3092	5055	1.63	0.5	0.04661	1.54	0.18681	2.17	0.02907	1.53	0.70	173.9	3.5	184.7	2.8	5.0	0.17
4	864	539	0.62	0.4	0.04813	1.75	0.18471	2.30	0.02783	1.50	0.65	172.1	3.7	177.0	2.6	4.8	0.22
5	1993	1466	0.74	0.0	0.04991	0.92	0.19948	1.76	0.02899	1.50	0.85	184.7	3.0	184.2	2.7	4.8	0.20
6	1738	1147	0.66	0.4	0.04831	1.36	0.18103	2.15	0.02718	1.66	0.77	168.9	3.3	172.8	2.8	5.3	0.18
7	2286	2007	0.88	0.2	0.04893	0.87	0.18634	1.74	0.02762	1.50	0.86	173.5	2.8	175.6	2.6	4.4	0.26
7	2011	1714	0.85	4.8	0.05215	3.73	0.21109	4.07	0.02936	1.65	0.40	194.5	7.2	186.5	3.0		
8	1734	2581	1.49	0.1	0.04892	0.93	0.18085	1.92	0.02681	1.68	0.88	168.8	3.0	170.6	2.8	4.9	0.20
9	1669	2079	1.25	0.1	0.04841	0.87	0.18631	1.75	0.02791	1.52	0.87	173.5	2.8	177.5	2.7	4.6	0.34
10	1824	1686	0.92	0.4	0.04666	1.41	0.16695	2.14	0.02595	1.61	0.75	156.8	3.1	165.2	2.6	4.9	0.25
11	807	575	0.71	0.1	0.04879	1.27	0.19305	1.97	0.02869	1.51	0.76	179.2	3.2	182.4	2.7	5.0	0.25
12	1747	2539	1.45	0.6	0.04616	1.47	0.17562	2.10	0.02759	1.51	0.72	164.3	3.2	175.5	2.6	5.4	0.16
13	3508	5644	1.61	0.2	0.04930	0.94	0.19470	1.78	0.02864	1.51	0.85	180.6	2.9	182.0	2.7	4.8	0.18
13	1816	11432	6.30	0.3	0.04850	1.06	0.18958	1.84	0.02835	1.50	0.82	176.3	3.0	180.2	2.7		
14	316	268	0.85	0.2	0.04854	1.66	0.19106	2.24	0.02855	1.51	0.67	177.5	3.7	181.5	2.7	5.4	0.29
15	3303	6149	1.86	1.5	0.04953	3.02	0.16749	3.41	0.02453	1.59	0.46	157.2	5.0	156.2	2.4	4.4	0.20
16	2283	2911	1.28	0.2	0.04873	1.12	0.15766	5.27	0.02346	5.15	0.98	148.7	7.3	149.5	7.6	5.1	0.24
17	2294	2295	1.00	0.0	0.05001	0.78	0.19960	1.69	0.02895	1.50	0.89	184.8	2.9	183.9	2.7	5.0	0.14
18	1501	3228	2.15	0.2	0.04848	1.02	0.18169	1.81	0.02718	1.50	0.83	169.5	2.8	172.9	2.6	5.0	0.20
18	877	1016	1.16	0.2	0.04922	1.26	0.19208	2.02	0.02831	1.57	0.78	178.4	3.3	179.9	2.8		
19	1485	3276	2.21	0.2	0.04812	1.14	0.18217	1.89	0.02746	1.50	0.80	169.9	3.0	174.6	2.6	5.3	0.21
20	1525	2750	1.80	0.1	0.04879	0.78	0.18309	1.92	0.02722	1.76	0.92	170.7	3.0	173.1	3.0	5.2	0.27
20	3278	6720	2.05	0.1	0.04981	0.87	0.18815	1.80	0.02739	1.58	0.88	175.1	2.9	174.2	2.7		
21	690	687	1.00	0.3	0.04937	2.74	0.16706	3.93	0.02454	2.82	0.72	156.9	5.7	156.3	4.4	5.4	0.21
22	617	437	0.71	0.1	0.04896	1.31	0.18504	1.99	0.02741	1.50	0.75	172.4	3.2	174.3	2.6	5.3	0.21
23	1186	1213	1.02	1.0	0.04449	2.76	0.16270	3.15	0.02652	1.52	0.48	153.1	4.5	168.7	2.5	4.9	0.19
23	1467	1589	1.08	0.0	0.04977	0.81	0.19465	1.74	0.02837	1.53	0.88	180.6	2.9	180.3	2.7		
24	1460	1373	0.94	0.1	0.04916	0.79	0.19130	1.70	0.02822	1.51	0.89	177.7	2.8	179.4	2.7	5.0	0.19
25	2846	2448	0.86	0.2	0.04846	1.49	0.19369	2.23	0.02899	1.66	0.74	179.8	3.7	184.2	3.0	4.9	0.25
26	1290	1724	1.34	0.5	0.04786	1.58	0.17403	2.20	0.02637	1.53	0.69	162.9	3.3	167.8	2.5	5.0	0.16
27	1593	1241	0.78	0.1	0.04852	1.50	0.18355	2.15	0.02744	1.54	0.72	171.1	3.4	174.5	2.7	5.0	0.20
27	2117	1235	0.58	0.0	0.05168	1.45	0.20405	2.59	0.02864	2.15	0.83	188.5	4.5	182.0	3.9		
28	891	650	0.73	0.1	0.04939	0.95	0.19137	1.88	0.02810	1.62	0.86	177.8	3.1	178.7	2.9	4.2	0.25
29	334	245	0.73	0.4	0.05077	2.47	0.19109	2.93	0.02730	1.57	0.54	177.6	4.8	173.6	2.7	5.3	0.27
30	577	392	0.68	5.5	0.05429	23.90	0.16522	24.02	0.02207	2.35	0.10	155.3	35.2	140.7	3.3	5.3	0.21
30	599	433	0.72	0.4	0.04963	2.89	0.18113	3.51	0.02647	2.00	0.57	169.0	5.5	168.4	3.3		

1049 Table 3. Molybdenite Re-Os data

Sample #	Wt (g)	Re (ppm)	±	^{187}Re (ppm)	±	^{187}Os (ppb)	±	Age	±*
313-460	0.014	143.32	1.08	90.08	0.39	24.17	0.09	16.11	0.06[0.08]
313-145	0.021	64.44	1.94	40.50	0.15	10.86	0.03	16.10	0.07[0.09]
001-640	0.010	104.16	1.32	65.47	0.33	17.56	0.08	16.10	0.07[0.09]
1605-334	0.039	224.51	1.55	141.11	0.47	37.64	0.10	16.01	0.06[0.08]
1605-155	0.018	221.57	1.18	139.26	0.54	36.97	0.12	15.93	0.06[0.08]
1605-33	0.012	323.60	2.27	203.39	0.92	53.82	0.22	15.88	0.06[0.08]

1050

1051 *Data are presented with (bracketed value) and without ^{187}Re decay constant uncertainty (Smoliar et

1052 al. (1996); Selby et al. (2007).

1053

1054 Table 4. Fluid inclusion assemblages (FIAs) and their respective microthermometric data
1055 temperatures

FIA No.	Characteristics	Homogenized to	$T_{homogenization}$ °C	Salinity wt% NaCl equiv	$T_{trapping}$ ˚C
Magmatic-hydrothermal transition					
1	liquid-vapor two-phase and vapor-rich two-phase fluid inclusions	liquid	340-360 °C	2-6 wt%	425
Potassic alteration stage					
2	halite-bearing fluid inclusions	liquid	419-436	50-52 wt%	425
3	halite-bearing fluid inclusions and vapor-rich two-phase fluid inclusions	halite dissolution vapor	388-405	41-45 wt% 4-7 wt%	398
4	vapor-rich two-phase fluid inclusions	liquid	385-400	1-6 wt%	390
5	vapor-rich two-phase fluid inclusions	liquid	360-370	1-6 wt%	380
6	liquid-vapor two-phase fluid inclusions,	liquid	335-355	2-7 wt%	360
Propylitic alteration stage					
7	liquid-vapor two-phase fluid inclusions	liquid	335-360	1-7 wt%	365
8	liquid-vapor two-phase fluid inclusions	liquid	318-332	2-7 wt%	340
9	liquid-rich two-phase fluid inclusions	liquid	270-290	2-11 wt%	290
Phyllic alteration stage					
10	liquid-vapor two-phase fluid inclusions	liquid	325-340	2-8 wt%	345
11	liquid-rich two-phase fluid inclusions	liquid	295-310	3-9 wt%	310
12	liquid-rich two-phase fluid inclusions	liquid	265-290	1-8 wt%	285

1056

Figure1

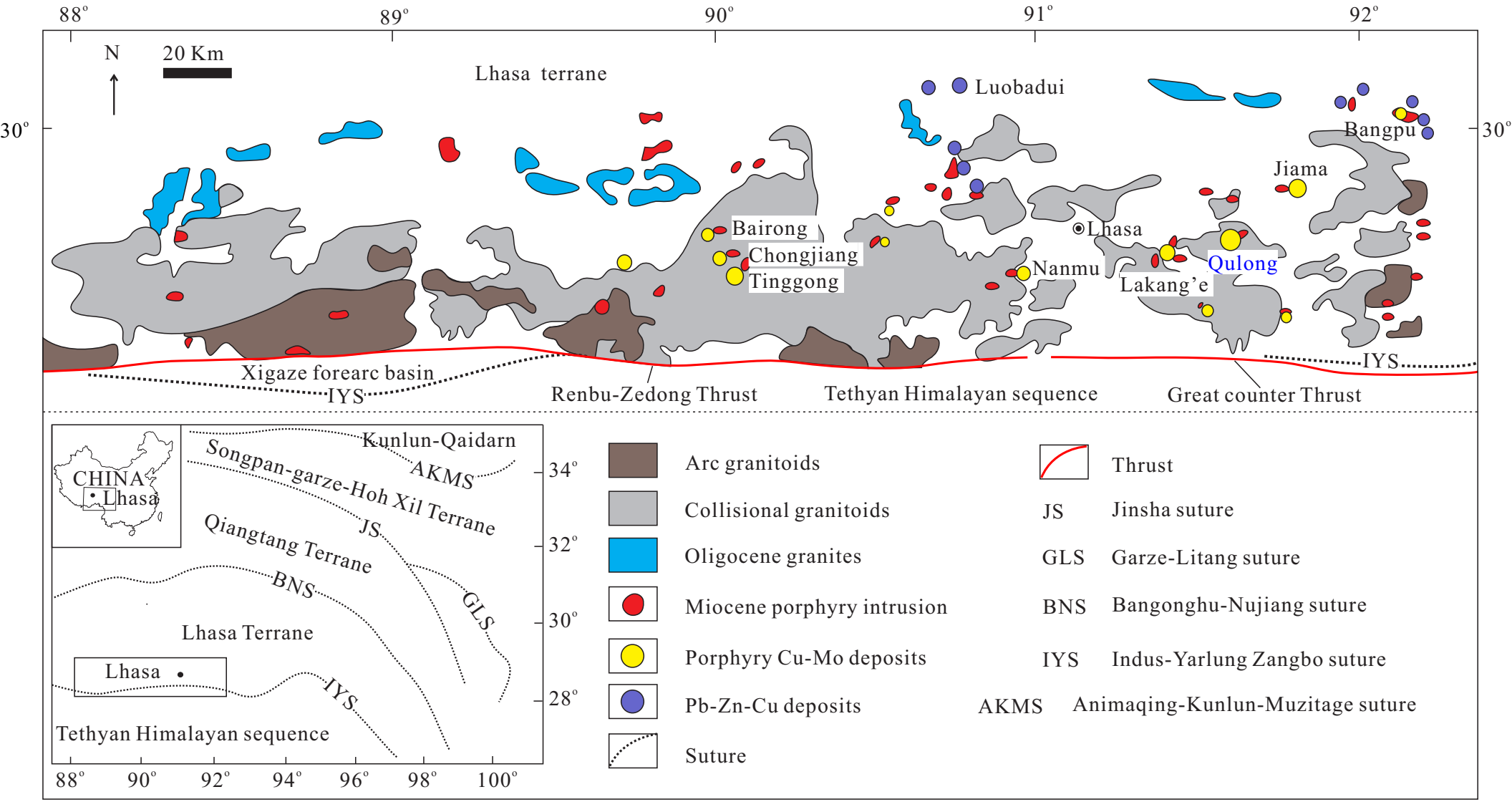
88°
89°
90°
91°
92°
N
20 Km
Lhasa terrane
30°
Luobadui
Bangpu
Jiama
Bairong
Chongjiang
Tinggong
Lhasa
Nanmu
Lakang'e
Qulong
Xigaze forearc basin
IYS
Renbu-Zedong Thrust
Tethyan Himalayan sequence
Great counter Thrust
CHINA
Lhasa
Kunlun-Qaidarn
AKMS
Songpan-garze-Hoh Xil Terrane
JS
Qiangtang Terrane
BNS
GLS
Lhasa Terrane
Lhasa
IYS
Tethyan Himalayan sequence
34°
32°
30°
28°
88°
90°
92°
94°
96°
98°
100°
Arc granitoids
Collisional granitoids
Oligocene granites
Miocene porphyry intrusion
Porphyry Cu-Mo deposits
Pb-Zn-Cu deposits
Suture
Thrust
JS Jinsha suture
GLS Garze-Litang suture
BNS Bangonghu-Nujiang suture
IYS Indus-Yarlung Zangbo suture
AKMS Animaqing-Kunlun-Muzitage suture

Figure2

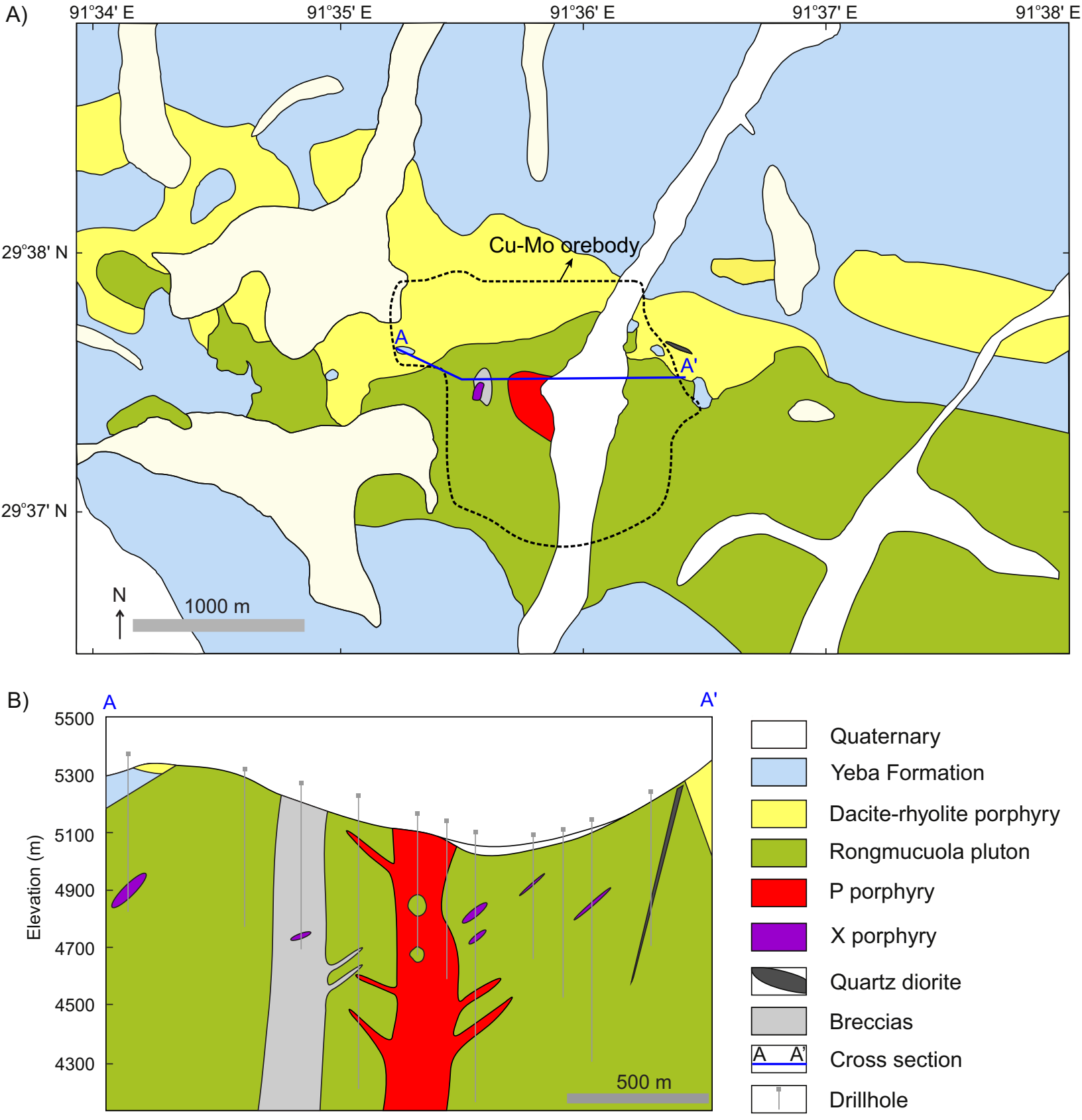
A)
91°34' E
91°35' E
91°36' E
91°37' E
91°38' E
29°38' N
29°37' N
Cu-Mo orebody
A
A'
N
1000 m
B)
A
A'
5500
5300
5100
4900
4700
4500
4300
Elevation (m)
500 m
Quaternary
Yeba Formation
Dacite-rhyolite porphyry
Rongmucuola pluton
P porphyry
X porphyry
Quartz diorite
Breccias
A A'
Cross section
Drillhole

Figure3

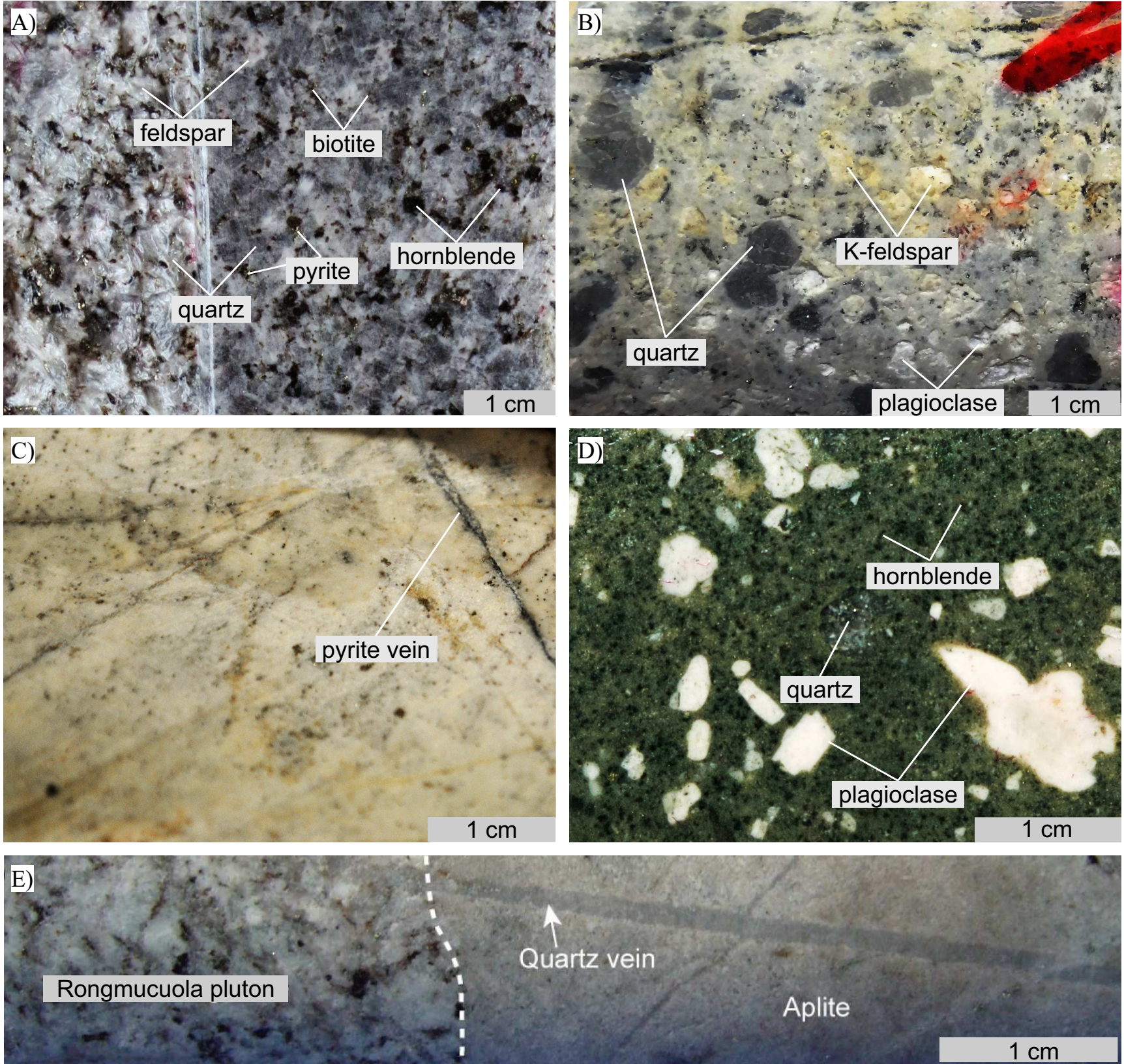
A)
feldspar
biotite
hornblende
pyrite
quartz
1 cm
B)
K-feldspar
quartz
plagioclase
1 cm
C)
pyrite vein
1 cm
D)
hornblende
quartz
plagioclase
1 cm
E)
Rongmucuola pluton
Quartz vein
Aplite
1 cm

Figure4

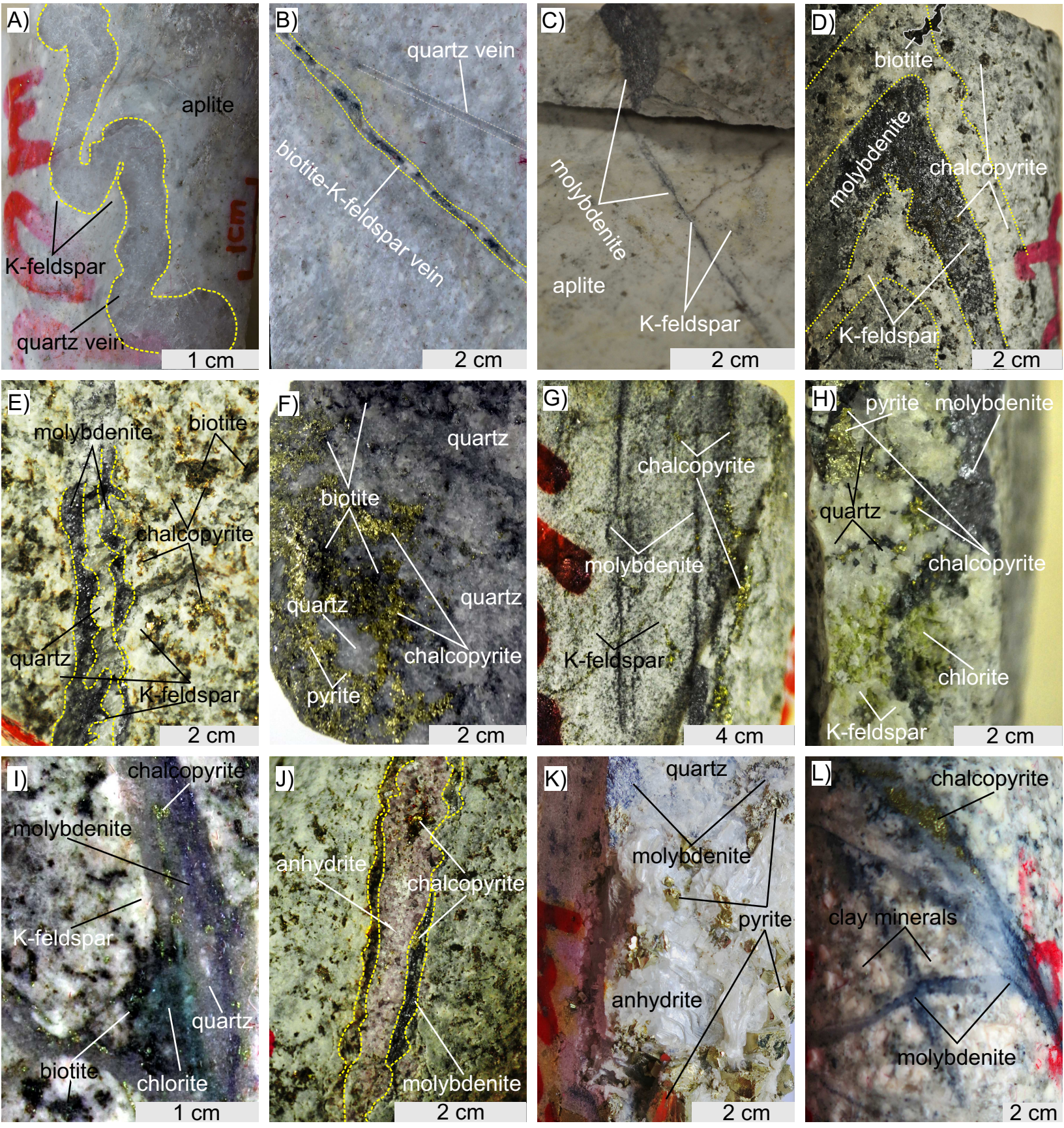
A)
aplite
K-feldspar
quartz vein
1 cm
B)
quartz vein
biotite-K-feldspar vein
2 cm
C)
molybdenite
aplite
K-feldspar
2 cm
D)
biotite
molybdenite
chalcopyrite
K-feldspar
2 cm
E)
molybdenite
biotite
chalcopyrite
quartz
K-feldspar
2 cm
F)
quartz
biotite
quartz
quartz
chalcopyrite
pyrite
2 cm
G)
chalcopyrite
molybdenite
K-feldspar
4 cm
H)
pyrite
molybdenite
quartz
chalcopyrite
chlorite
K-feldspar
2 cm
I)
chalcopyrite
molybdenite
K-feldspar
quartz
biotite
chlorite
1 cm
J)
anhydrite
chalcopyrite
molybdenite
2 cm
K)
quartz
molybdenite
pyrite
anhydrite
2 cm
L)
chalcopyrite
clay minerals
molybdenite
2 cm

Figure5

Click here to download Figure Fig 5_New.tif

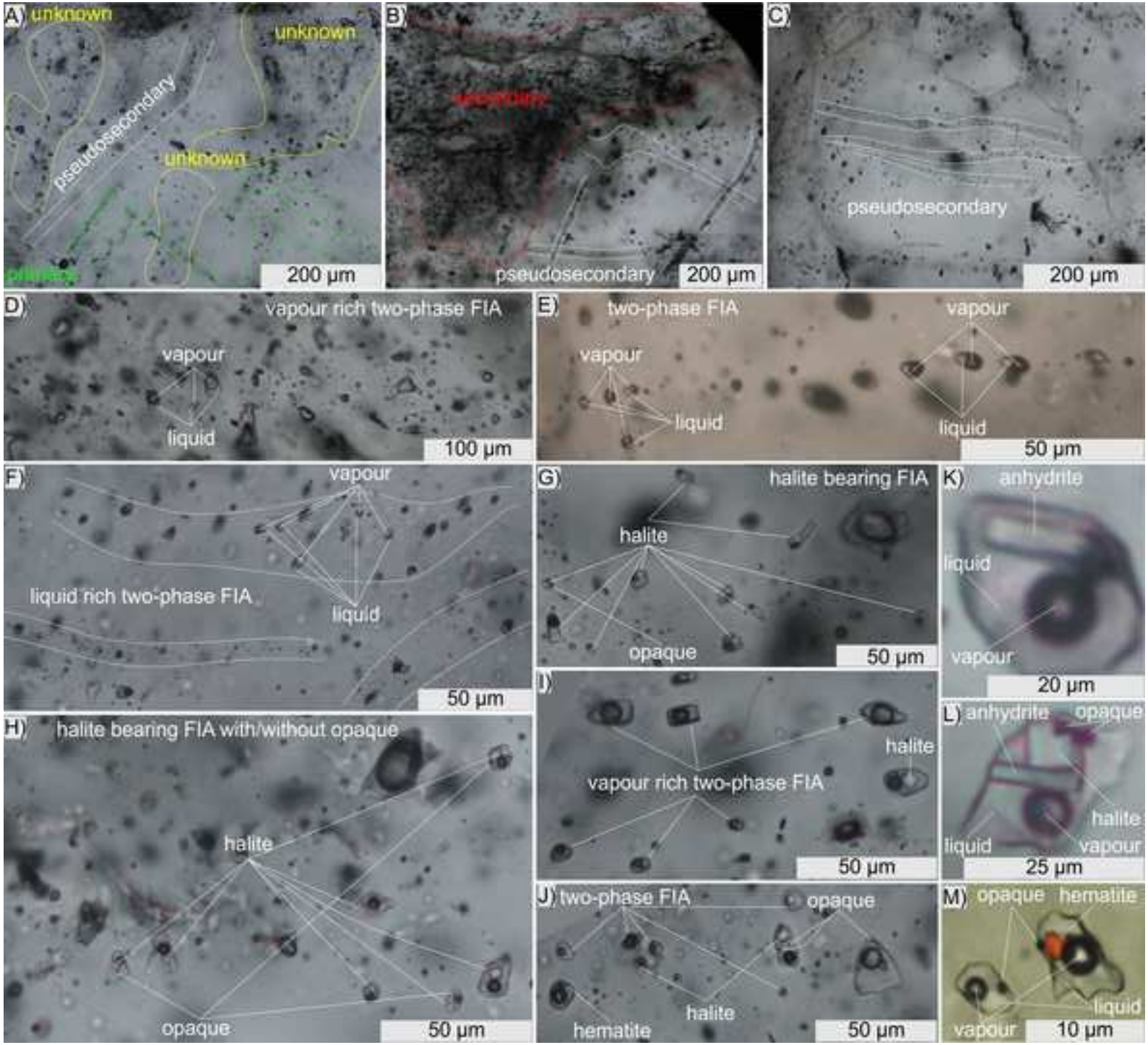

Figure6

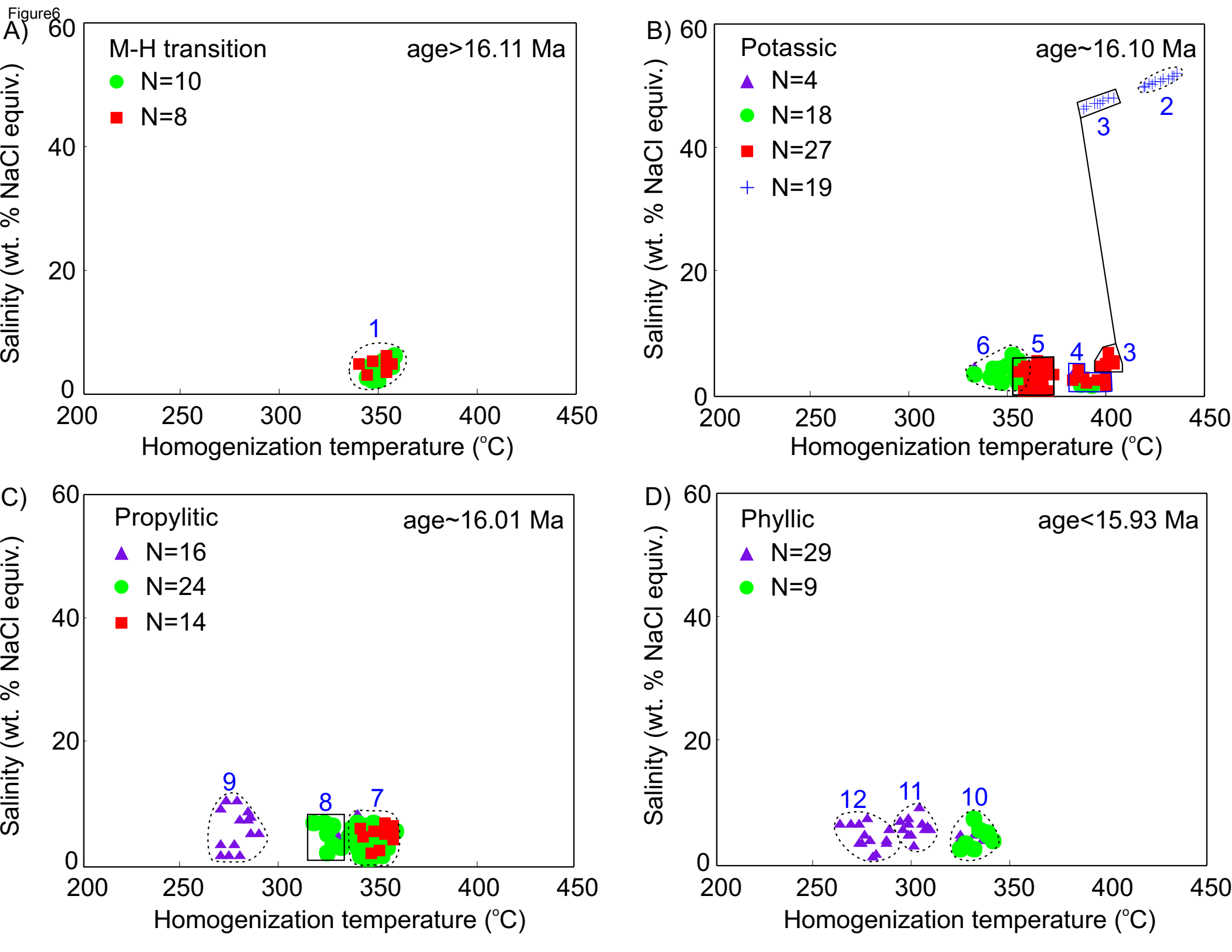
A)
M-H transition
age>16.11 Ma
N=10
N=8
1
B)
Potassic
age~16.10 Ma
N=4
N=18
N=27
N=19
2
3
4
5
6
C)
Propylitic
age~16.01 Ma
N=16
N=24
N=14
7
8
9
D)
Phyllic
age<15.93 Ma
N=29
N=9
10
11
12
Salinity (wt. % NaCl equiv.)
Homogenization temperature (°C)
0
20
40
60
200
250
300
350
400
450

Figure7

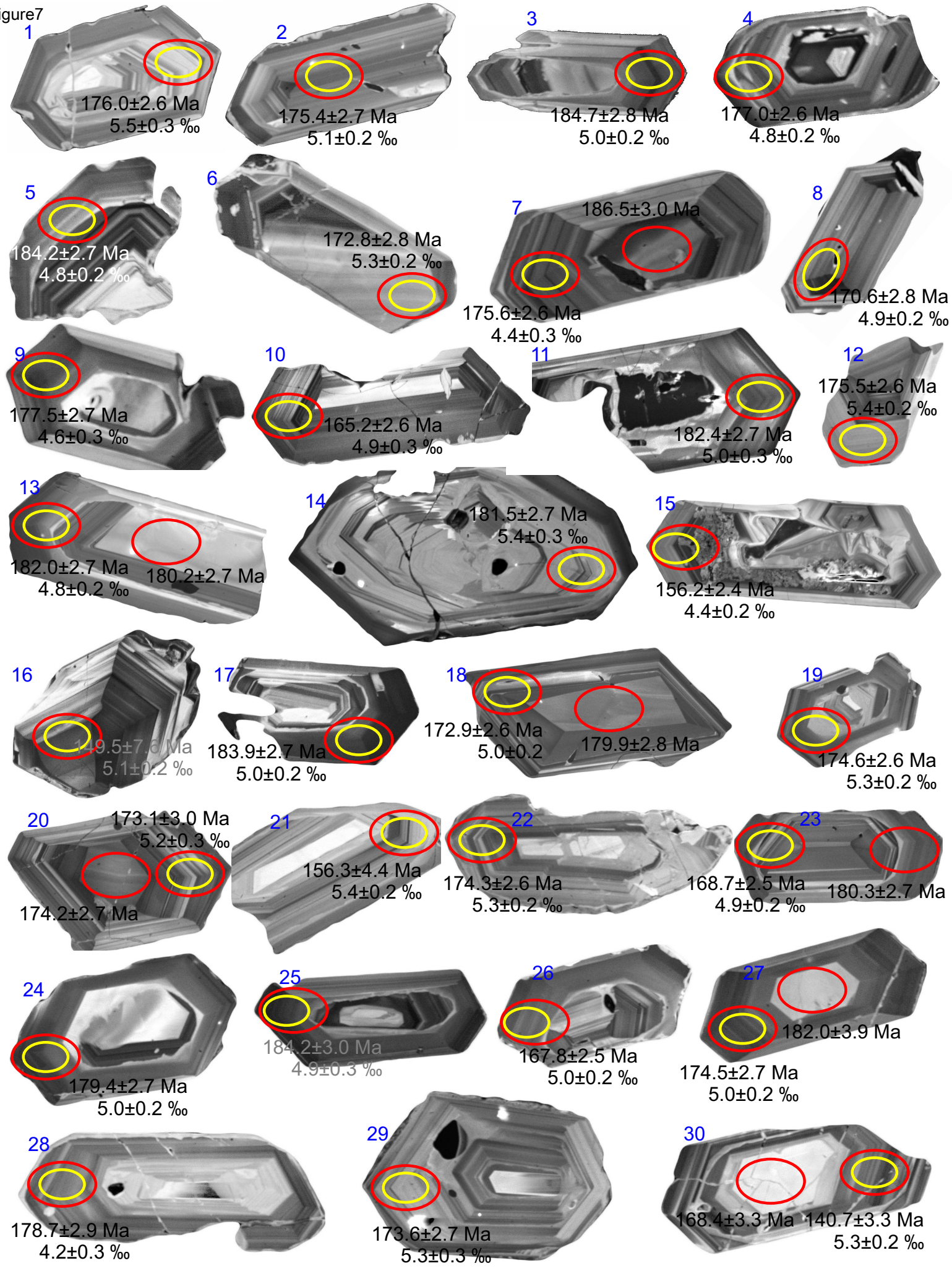
1
176.0±2.6 Ma
5.5±0.3 ‰
2
175.4±2.7 Ma
5.1±0.2 ‰
3
184.7±2.8 Ma
5.0±0.2 ‰
4
177.0±2.6 Ma
4.8±0.2 ‰
5
184.2±2.7 Ma
4.8±0.2 ‰
6
172.8±2.8 Ma
5.3±0.2 ‰
7
186.5±3.0 Ma
175.6±2.6 Ma
4.4±0.3 ‰
8
170.6±2.8 Ma
4.9±0.2 ‰
9
177.5±2.7 Ma
4.6±0.3 ‰
10
165.2±2.6 Ma
4.9±0.3 ‰
11
182.4±2.7 Ma
5.0±0.3 ‰
12
175.5±2.6 Ma
5.4±0.2 ‰
13
182.0±2.7 Ma
4.8±0.2 ‰
180.2±2.7 Ma
14
181.5±2.7 Ma
5.4±0.3 ‰
15
156.2±2.4 Ma
4.4±0.2 ‰
16
149.5±7.6 Ma
5.1±0.2 ‰
17
183.9±2.7 Ma
5.0±0.2 ‰
18
172.9±2.6 Ma
5.0±0.2
179.9±2.8 Ma
19
174.6±2.6 Ma
5.3±0.2 ‰
20
173.1±3.0 Ma
5.2±0.3 ‰
174.2±2.7 Ma
21
156.3±4.4 Ma
5.4±0.2 ‰
22
174.3±2.6 Ma
5.3±0.2 ‰
23
168.7±2.5 Ma
4.9±0.2 ‰
180.3±2.7 Ma
24
179.4±2.7 Ma
5.0±0.2 ‰
25
184.2±3.0 Ma
4.9±0.3 ‰
26
167.8±2.5 Ma
5.0±0.2 ‰
27
182.0±3.9 Ma
174.5±2.7 Ma
5.0±0.2 ‰
28
178.7±2.9 Ma
4.2±0.3 ‰
29
173.6±2.7 Ma
5.3±0.3 ‰
30
168.4±3.3 Ma
140.7±3.3 Ma
5.3±0.2 ‰
30um
170 Ma U-Pb analysis spots and $^{206}Pb/^{238}U$ages
4.5 $\delta^{18}O$ analysis spots and values

Figure8

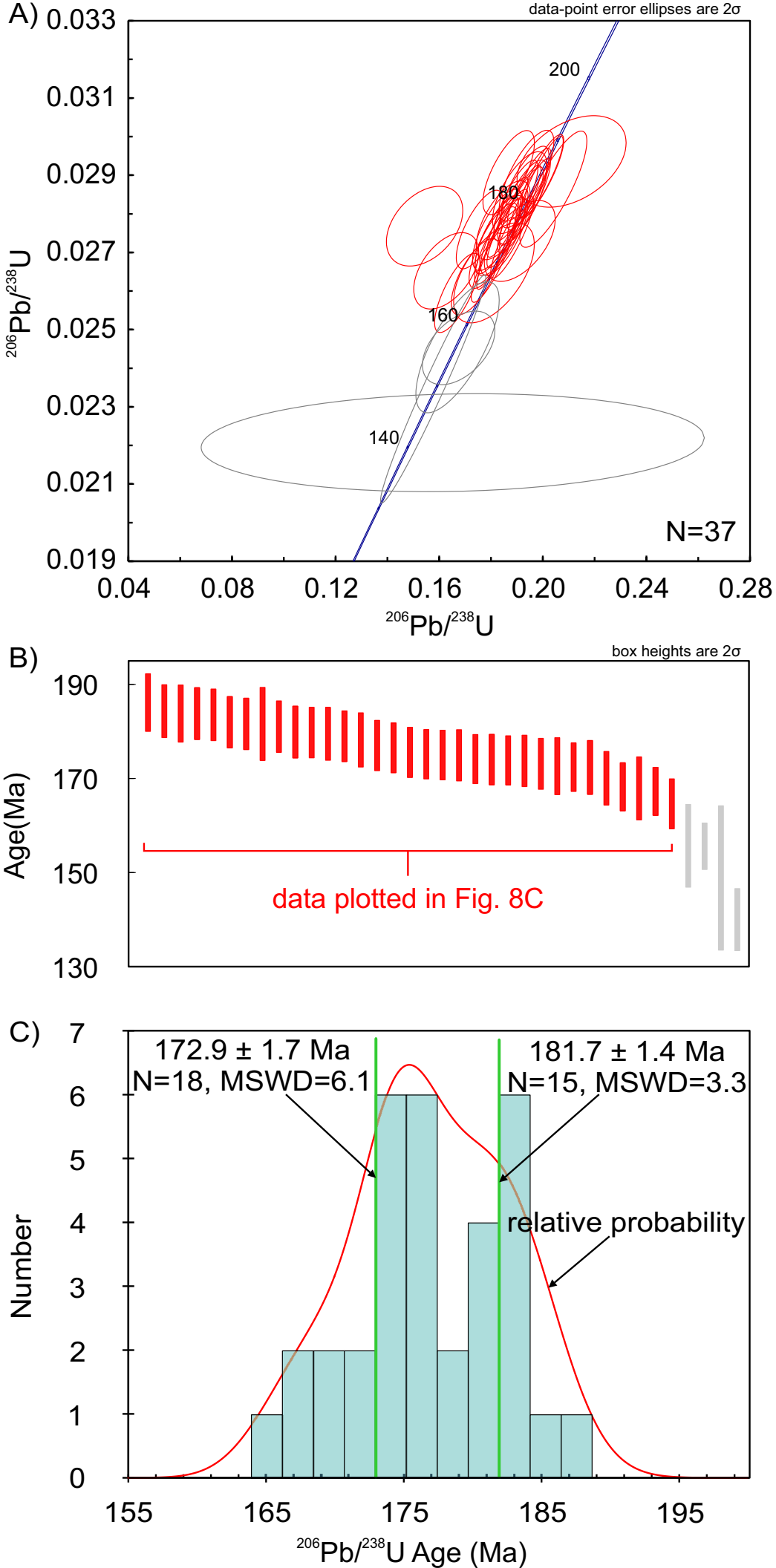
A)
data-point error ellipses are 2σ
200
180
160
140
N=37
0.033
0.031
0.029
0.027
0.025
0.023
0.021
0.019
0.04
0.08
0.12
0.16
0.20
0.24
0.28
206Pb/238U
B)
box heights are 2σ
190
170
150
130
Age(Ma)
data plotted in Fig. 8C
C)
172.9 ± 1.7 Ma
N=18, MSWD=6.1
181.7 ± 1.4 Ma
N=15, MSWD=3.3
relative probability
Number
7
6
5
4
3
2
1
0
155
165
175
185
195
206Pb/238U Age (Ma)

Figure9

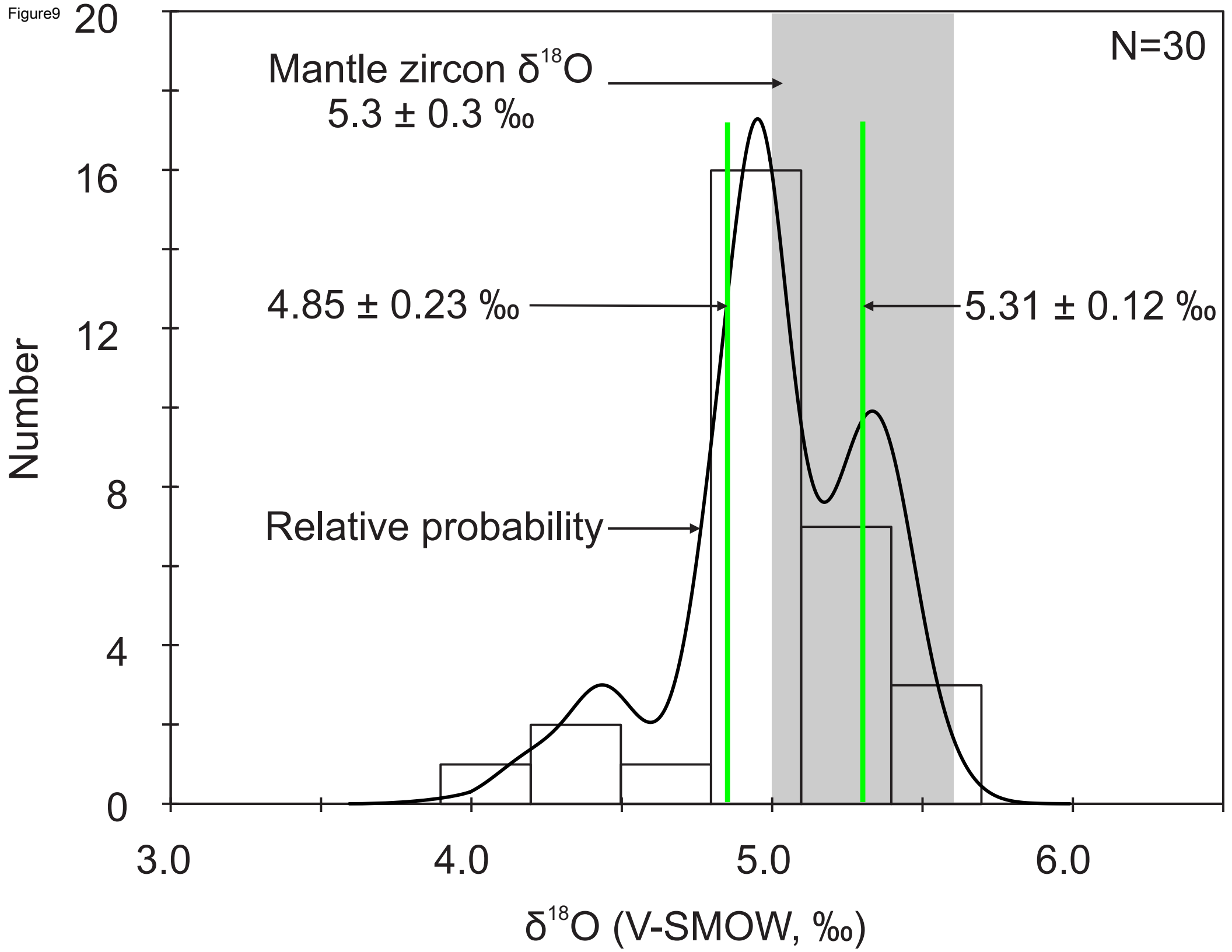
N=30
Mantle zircon δ18O
5.3 ± 0.3 ‰
4.85 ± 0.23 ‰
5.31 ± 0.12 ‰
Relative probability
Number
20
16
12
8
4
0
3.0
4.0
5.0
6.0
δ18O (V-SMOW, ‰)

Figure10

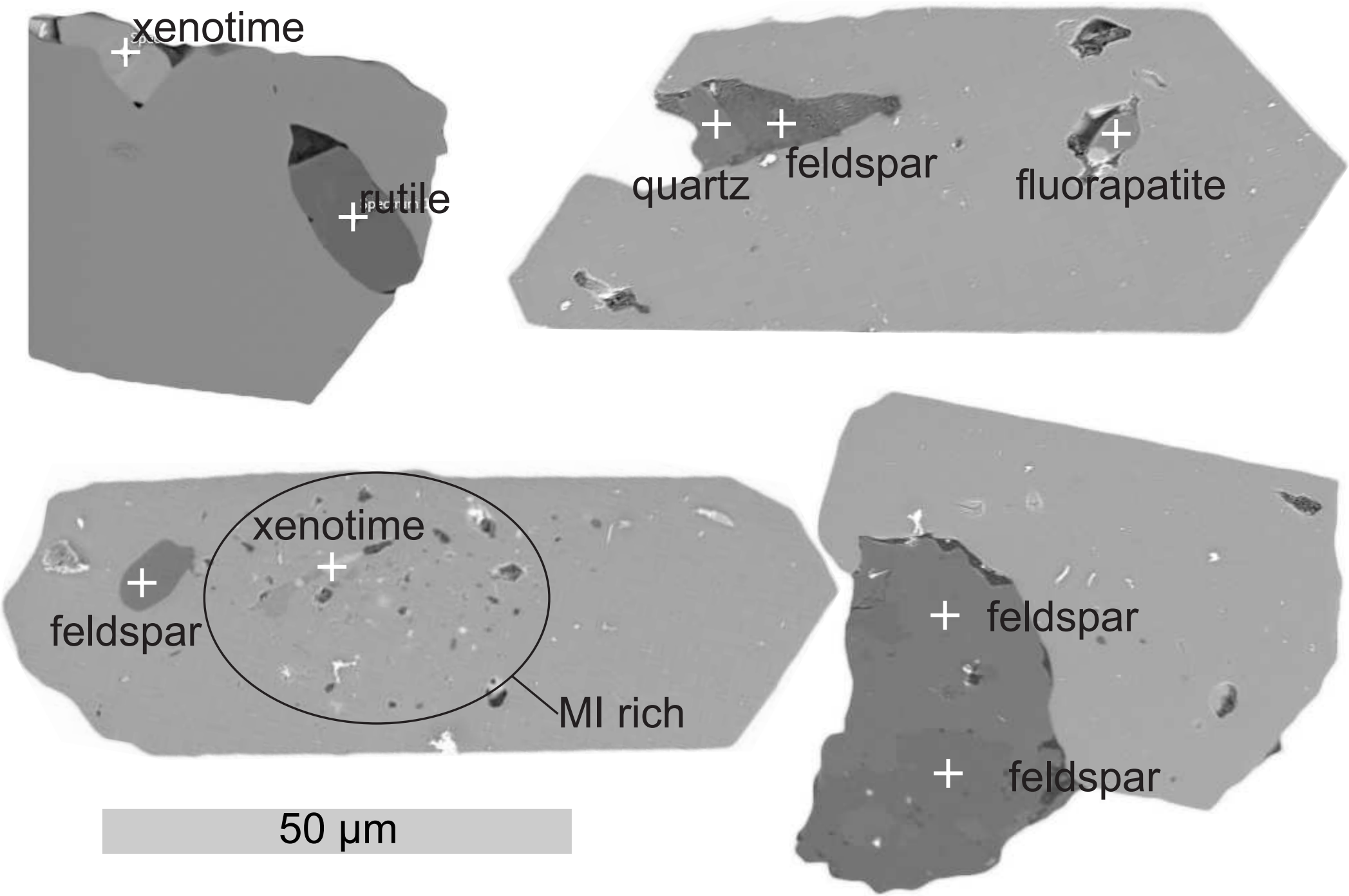
xenotime
rutile
quartz
feldspar
fluorapatite
xenotime
feldspar
MI rich
feldspar
feldspar
50 µm

Figure11

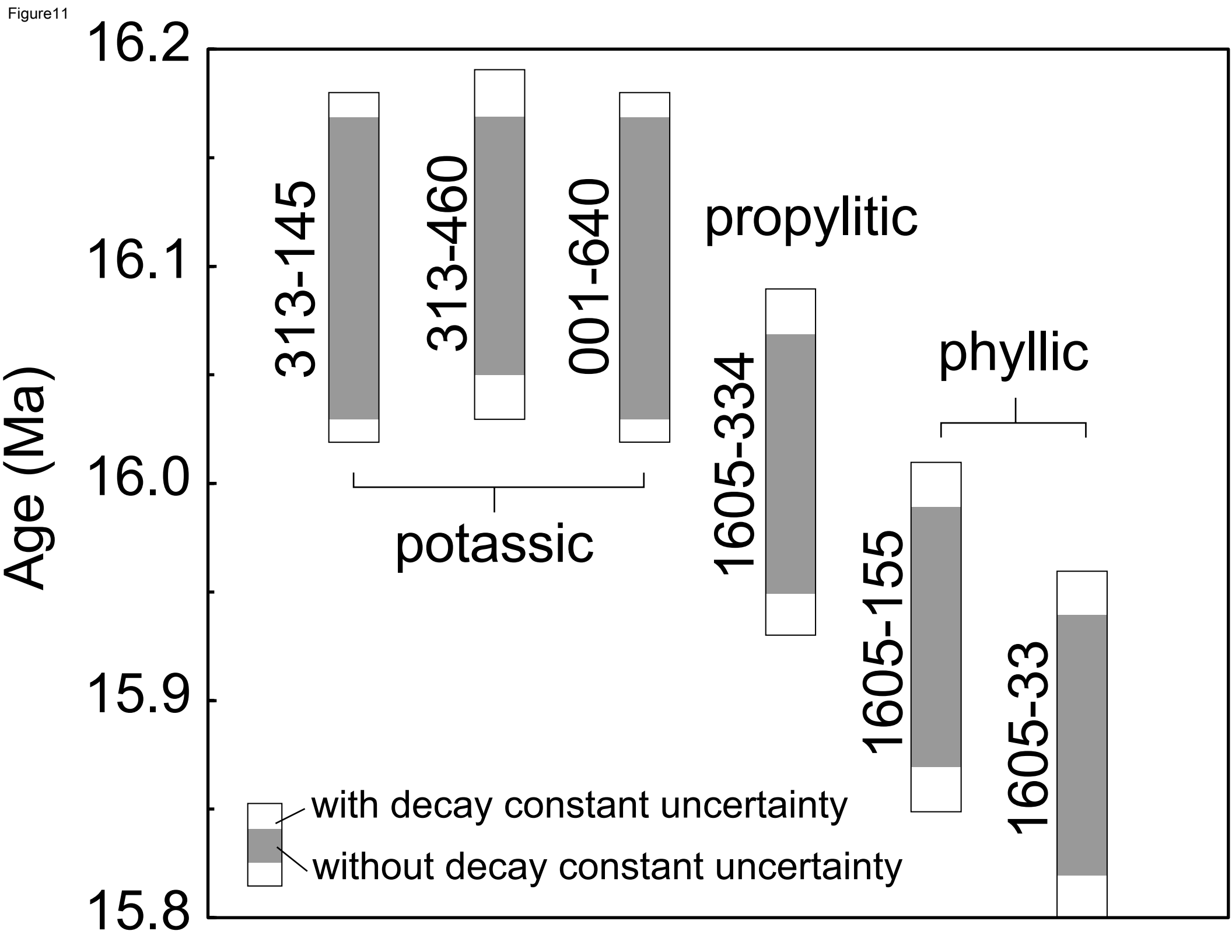
16.2
16.1
16.0
15.9
15.8
Age (Ma)
313-145
313-460
001-640
potassic
propylitic
1605-334
phyllic
1605-155
1605-33
with decay constant uncertainty
without decay constant uncertainty

Figure12

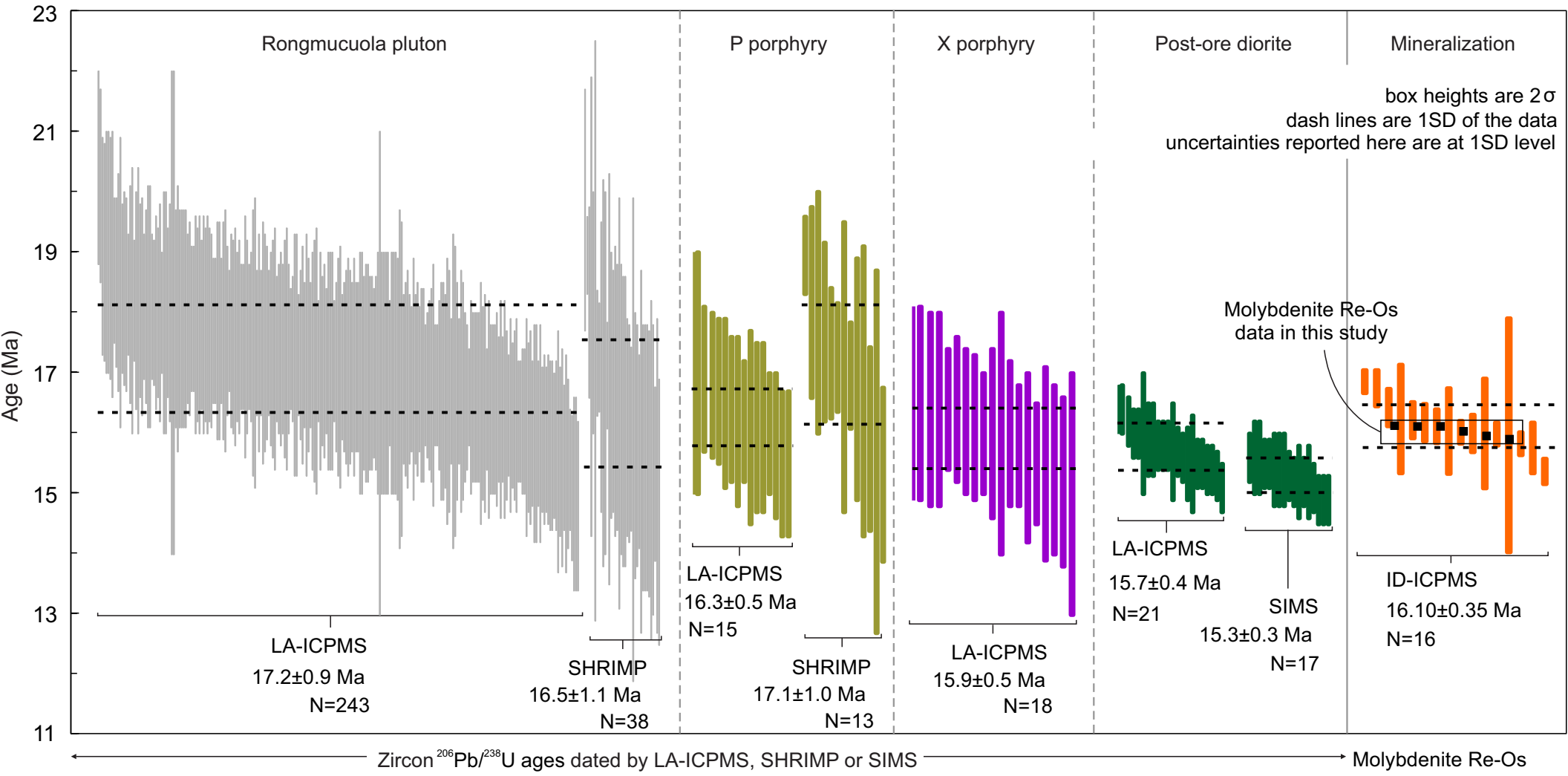
Rongmucuola pluton
P porphyry
X porphyry
Post-ore diorite
Mineralization
box heights are 2σ
dash lines are 1SD of the data
uncertainties reported here are at 1SD level
Molybdenite Re-Os
data in this study
Age (Ma)
23
21
19
17
15
13
11
LA-ICPMS
17.2±0.9 Ma
N=243
SHRIMP
16.5±1.1 Ma
N=38
LA-ICPMS
16.3±0.5 Ma
N=15
SHRIMP
17.1±1.0 Ma
N=13
LA-ICPMS
15.9±0.5 Ma
N=18
LA-ICPMS
15.7±0.4 Ma
N=21
SIMS
15.3±0.3 Ma
N=17
ID-ICPMS
16.10±0.35 Ma
N=16
Zircon $^{206}Pb/^{238}U$ ages dated by LA-ICPMS, SHRIMP or SIMS
Molybdenite Re-Os

Figure13

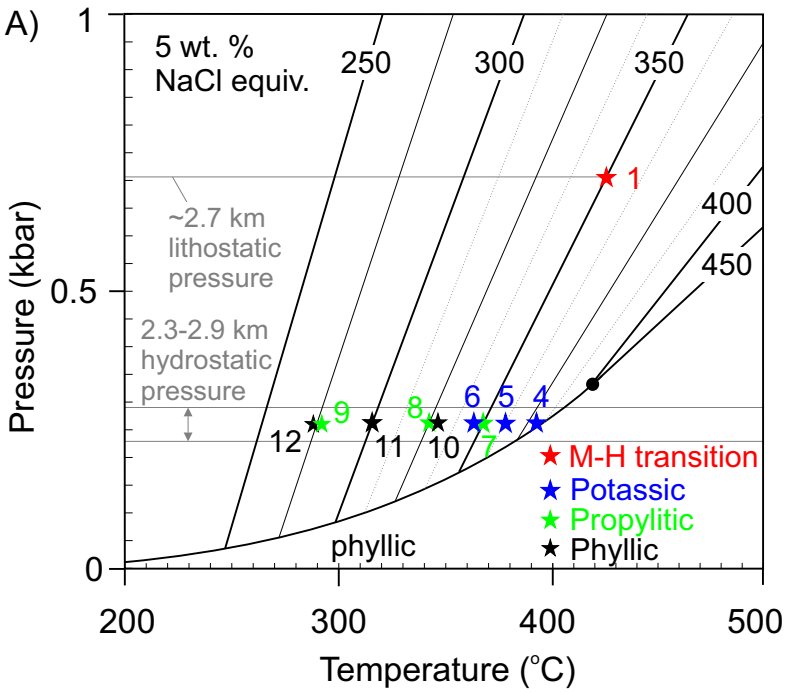
A)
5 wt. %
NaCl equiv.
250
300
350
400
450
~2.7 km
lithostatic
pressure
2.3-2.9 km
hydrostatic
pressure
1
2
3
4
5
6
7
8
9
10
11
12
M-H transition
Potassic
Propylitic
Phyllic
phyllic
Pressure (kbar)
Temperature (°C)
0
0.5
1
200
300
400
500

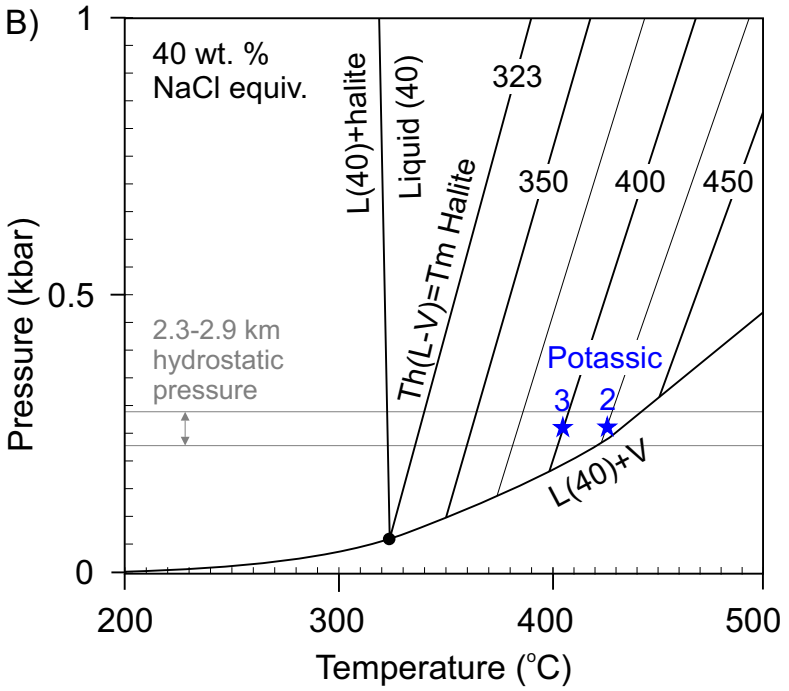
B)
40 wt. %
NaCl equiv.
L(40)+halite
Liquid (40)
Th(L-V)=Tm Halite
323
350
400
450
2.3-2.9 km
hydrostatic
pressure
Potassic
3
2
L(40)+V
Pressure (kbar)
Temperature (°C)
0
0.5
1
200
300
400
500

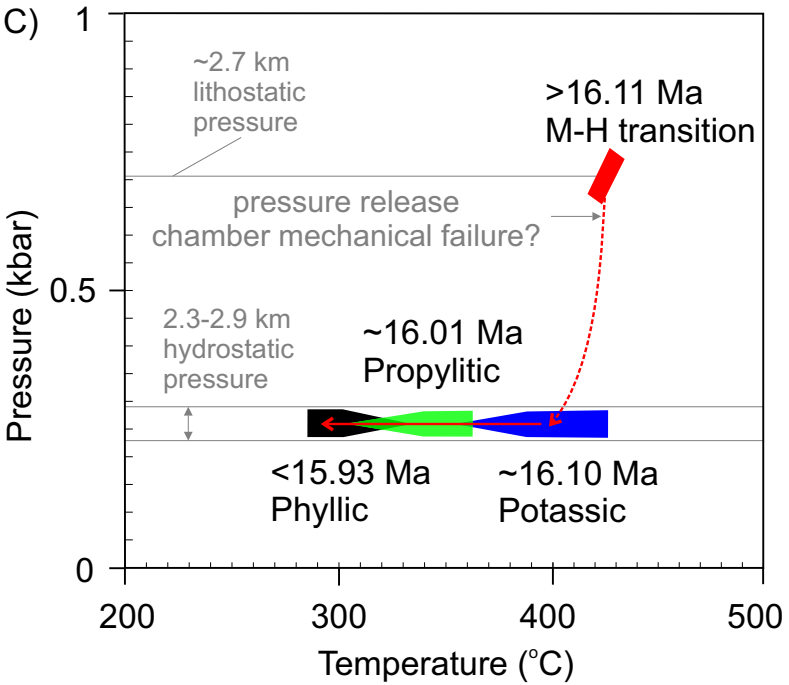
C)
~2.7 km
lithostatic
pressure
>16.11 Ma
M-H transition
pressure release
chamber mechanical failure?
2.3-2.9 km
hydrostatic
pressure
~16.01 Ma
Propylitic
<15.93 Ma
Phyllic
~16.10 Ma
Potassic
Pressure (kbar)
Temperature (°C)
0
0.5
1
200
300
400
500